Universidade de São Paulo
Instituto de Física

Espectroscopia de absorção de raios-X dos arseniatos de ferro Ba(Fe$_{1-x}$T$_x$)$_2$As$_2$, (T = Mn, Co, x = 0.0 e x = 0.08)

Alvaro Godoy de Figueiredo

Orientador: Prof. Dr. Fernando Assis Garcia
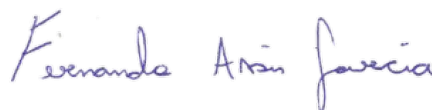Coorientador: Prof. Dr. Ricardo Donizeth dos Reis

Dissertação de mestrado apresentada ao Instituto de Física da Universidade de São Paulo, como requisito parcial para a obtenção do título de Mestre(a) em Ciências.

Banca Examinadora:
Prof. Dr. Fernando Assis Garcia - Orientador (IFUSP)
Prof. Dr. Leandro Felix de Sousa Bufaiçal (UFG)
Profa. Dra. Letície Mendonça Ferreira (UFABC)

São Paulo
2021

University of São Paulo

Physics Institute

X-ray absorption spectroscopy of the iron arsenides Ba(Fe$_{1-x}$T$_x$)$_2$As$_2$, (T = Mn, Co, x = 0.0 and x = 0.08)

Alvaro Godoy de Figueiredo

Supervisor: Prof. Dr. Fernando Assis Garcia
Co-advisor: Prof. Dr. Ricardo Donizeth dos Reis

Masters dissertation submitted to the Physics Institute of the University of São Paulo, as a partial fulfillment of the requirements for the degree of Master of Science.

Examination Committee:
Prof. Dr. Fernando Assis Garcia - Supervisor (IFUSP)
Prof. Dr. Leandro Felix de Sousa Bufaiçal (UFG)
Prof. Dr. Letície Mendonça Ferreira (UFABC)

São Paulo

2021

Agradecimentos

Quero agradecer aos meus pais, Alvaro e Solange, e ao meu irmão Gabriel, por todo suporte, pela paciência, compreensão e motivação diária durante todos esses anos. Obrigado por me proporcionarem essa oportunidade única.

Quero agradecer ao meu orientador Prof. Dr. Fernando Assis Garcia, pelo aprendizado adquirido, orientação e auxílio desda graduação. Por toda paciência, discussões e noites em claro fazendo experimentos permeados por café.

Juntamente quero agradecer ao meu co-orientador Prof. Dr. Ricardo Donizeth dos Reis, por ter me aceito em seu projeto no Sirius, onde também cresci tanto pessoalmente como profissionalmente.

Ambos foram de grande importância para o surgimento dessa oportunidade de contribuir para um projeto tão especial.

Estendo ainda para a equipe de alunos do Prof. Dr. Ricardo Donizeth dos Reis e dos funcionários do CNPEM, com os quais passei meses discutindo sobre diversas instrumentações.

Também agradeço à Profa. Dra. Cris Adriano da Universidade Estadual de Campinas (UNICAMP) e seu grupo, que sintetizaram as amostras estudadas neste trabalho, além do auxílio na tomada de medidas.

Quero agradecer à atlética AAAGW e sua equipe de jiu-jitsu, me mostrando que manter atividades físicas pareadas com os estudos têm um grade papel na saúde, além das amizades adquiridas. Também uma das melhores decisões que já tomei.

Agradecer ao Laboratório Nacional de Luz Síncroton (LNLS) no CNPEM, em Campinas, pela utilização de suas instalações para a parte experimental que é o corpo principal deste trabalho e pelo suporte durante o projeto da célula de pressão.

Quero também agradecer à minhas professoras de físca durante o ensino médio, Edna e Luciana, que cultivaram essa minha curiosidade desde início, tenha sido através das aulas, discussões, cursos ou olimpíadas.

Abstract

This master dissertation is dedicated to two topics. The first is discussed in the main body of the text and concerns X-ray absorption spectroscopy (XAS) experiments of selected iron-based superconducting (IBS) materials. The second is discussed in Appendix A, and concerns our instrumentation work with an optimized design for a "panoramic" pressure cell.

The first chapter is dedicated to introduce some theoretical concepts related to the field of the IBS materials. The second chapter introduces the XAS technique, an overview about XAS of IBS materials, and general topics related to our experimental analyses. In the third chapter, our experimental data are presented and discussed and in chapter four we give our conclusions.

To a large extent, we dedicate our work to the polarization dependence of the near edge x-ray absorption spectroscopy (XANES). This is an element specific probe to the real space distribution of the density of unoccupied states in solid state materials. We probe the Fe and As K-edges of $Ba(Fe_{1-x}M_x)_2As_2$ ($M = $ Mn, Co and $x = 0.0$ and 0.08). The experiments reveal a strong polarization dependence of the probed XANES spectra, which concerns mainly an increase of the intensity of electronic transitions when the beam polarization is set out of the sample ab crystallographic plane. The results show that states with p_z orbital character dominate the density of unoccupied states close to the Fermi level. Partial substitution of Fe by Co is shown to decrease the anisotropy intensity, suggesting that Co doping donate electrons preferentially to states with p_z orbital character. On the other hand, Mn substitution causes the increase of the p_z orbital anisotropy, which is proposed to take place by means of an enhanced local Fe3d4p mixing, unveiling the role of Fe4p states in the localization of the Fe3d orbitals. Moreover, by comparing our results to previous experiments, we identify the relative mixing between Fe and the pnictide $4p_{x,y,z}$ orbitals as a clear divide between the electronic properties of iron arsenides and selenides. Our conclusions are supported by polarization dependent FEFF calculations of the XANES spectra and by quantum chemistry calculations of the orbital states electronic structure of the Fe coordination.

The above discussed, composes the main body of the work. In the Appendix A, we present an optimized Diamond Anvil Cell (DAC) design, to be used for high-pressure experiments adopting x-ray scattering geometry. This new design brings greater angle opening on a reflection geometry, as well as smaller size and mass, essential for low-temperature experiments. It was designed to be used in the CNPEM facilities.

Resumo

Essa dissertação de mestrado é dedicada à dois tópicos. O primeiro é discutido na maior parte do texto and refere-se à experimentos de espectroscopia de absorção de raios-x (XAS) dos materiais selecionados classificados como Supercondutores Baseados em Ferro (IBS). Já o segundo tópico é discutido no Apêndice A, e compreende o trabalho de instrumentação com um design otimizado de uma célula "panorâmica" de pressão.

O primeiro capítulo é dedicado à introdução de alguns conceitos teóricos relacionados ao campo dos materiais IBS. O segundo capítulo introduz a técnica de XAS em IBS, além de tópicos gerais relacionados à nossas análises experimentais. Já no terceiro capítulo, nossos dados experimentais são apresentados e discutidos, e no capítulo quarto são dadas nossas conclusões.

Boa parte deste trabalho é dediacda à dependência com polarização da espectroscopia de raios-x próxima à borda de absorção (XANES), um método que sonda a distribuição de densidade de estados desocupados num elemento específico em materias sólidos. Sondamos as bordas K do Fe e do As do Ba(Fe$_{1-x}$M$_x$)$_2$As$_2$ ($M =$ Mn, Co e $x = 0.0$ e 0.08). O experimento revela uma forte dependência com a polarização através dos espectros de XANES, que essencialmente mostram um aumento da intensidade de transições eletrônicas quando a polarização do feixe está direcionada para fora do plano cristalográfico ab da amostra. Esses resultados mostram que estados com caráter dos orbitais p_z dominam a densidade do estados desocupados próximos ao nível de Fermi. Substituição parcial do Fe pelo Co mostra uma diminuição na intensidade da anisotropia, sugeringo que a dopagem por Co doa elétrons preferencialmente para estados com caráter do orbital p_z. Por outro lado, substituição por Mn gera um aumento da anisotropia do orbital p_z, que é proposto ser causado através dum aumento da hibridização Fe$3d4p$, revelando o papel dos estados Fe$4p$ na localização dos orbitais Fe$3d$. Além disso, comparando com os resultados de experimentos anteriores, foi possível identificar a hibridização relativa entre os orbitais $4p_{x,y,z}$ do Fe e do pnictídeo como uma clara divisão entre as propriedades eletrônicas do selenatos e arseniatos de ferro. Nossas conclusões são suportadas por cálculos do espectro de XANES através de FEFF dependentes de polarização e por cálculos de química quântica dos estados eletrônicos dos orbitais da coordenação do Fe.

O que foi discutido acima compõe o corpo principal do trabalho, enquanto que uma segundo tema diferente é adicionado no Apêndice A, apresentando um design de Célula de Bigorna de Diamante (DAC) mais otimizado, que são usadas para experimentos em alta pressão pareados

com raios-x. Esse novo design traz uma maior abertura angular numa montagem de reflexão, assim como um menor tamanho e massa, essenciais para experimento em baixa temperatura. Foi desenhada para ser utilizada nas dependências do CNPEM.

Palavras-chave: supercondutores de alta temperatura; supercondutores baseados em ferro; espectroscopia de absorção de raios-x; célula de bigorna de diamente.

Contents

List of Figures

Chapter 1

Introduction

Magnetism is an incredible and important phenomenon, leading to many advances in our understanding about condensed matter physics and technology breakthroughs. On pair with magnetism, is the phenomenon of superconductivity, which is also a great source of new physics and applications. A little more than a decade ago, Kamihara *et al.*[1] discovered a new family of materials that can express superconductivity through magnetic fluctuations, namely the *Iron Based Superconductors* (IBS).

The connection between both phases was already known in the context of the copper oxide [2] and heavy fermion families of superconductors. The later case, is the prime example of high T_c superconductors, thus inciting studies on the new IBS family. Besides the potential for applications, superconductivity in the IBS, as in the copper oxides family, do not fit into the BCS theory for superconductors, increasing further the incentive for research on the field.

In this work we want to probe the electronic structure of $Ba(Fe_{1-x}T_x)_2As_2$ (*T = Mn, Co*) single crystals for different doping values, by means of polarization dependent *X-ray Absorption Spectroscopy* (XAS) at *Fe* and *As K* edges. We employed a linearly polarized beam and mounted our sample in a 6+2 circle diffractometer. In this experimental setup, new selection rules are imposed to the XAS process, allowing us to disentangle the element specific orbital the contribution to the XAS spectra. Our experiments could provide insights on the material Fermi surface orbital composition as well as on the distribution of electrons and holes added by doping. Multiple scattering simulations were implemented by the FEFF 8.4 code also were also performed and helped us with the experiment interpretation.

In this chapter, we go through some important concepts and ideas related to our work. We start discussing the idea of itinerant magnetism, electronic structure and superconductivity. We review some results on the field of the IBS and present a review on the literature about XAS of IBS materials.

The first step is to understand how magnetism can arise (or not) from electron-electron interaction, and that's the proposal from the most important model of interacting electrons in modern condensed matter physics, the Hubbard Model [11, 12], (formulated by the British physicist John Hubbard in 1963), whose most simple formulation (one band, one dimension) is

written as:

$$\hat{\mathcal{H}}_H = -t \sum_{i,\sigma} \left(\hat{c}_{i,\sigma}^\dagger \hat{c}_{i+1,\sigma} + \hat{c}_{i+1,\sigma}^\dagger \hat{c}_{i,\sigma} \right) + U \sum_i \hat{n}_{i\uparrow} \hat{n}_{i\downarrow} \tag{1.1}$$

where t is the hopping integral, $\hat{c}_{i,\sigma}^\dagger \hat{c}_{i+1,\sigma}$ destroys an electron in the lattice site index $i{+}1$ with spin σ and creates it back in the lattice site index i (or vice-versa), U is the strength of on-site electron interaction, and $\hat{n}_i = \hat{c}_{i,\sigma}^\dagger \hat{c}_{i,\sigma}$ is the occupation number operator for each spin. Therefore the first sum contains information about the kinetic energy of electrons (hopping between atoms), while the second is the interaction energy via Coulomb repulsion between the electrons.

Both terms compete, the first leading to a metallic behaviour by delocalizing electrons into itinerant states (Bloch states), while the second leads to an insulating state due to electron localization. Hence we can split the results into two extreme categories according to the electronic states localization degree, known as localized (large U) and itinerant (large t) spin magnetism.

Representative of the former magnets are the transition metal oxides (usually MO_n, where M is a transition metal, O is the oxygen and n is the coordination number) [4]. Here, both the coordination geometry and the properties of the ligands have great influence over the localized spin interactions [5, 6]. Transition metal oxides have a tendency to display antiferromagnetism and, moreover, are insulating materials even in the case of half-filled bands (being called Mott insulators).

Now, for the latter itinerant spin magnets, typical of metals [10], extreme examples include either the ferromagnetic materials $ZrZn_2$ and Sc_3In [7, 8] or the antiferromagnetic material ($AuTi$ [9]). These examples are extreme, in the sense that although we can't associate a magnetic moment to each atom specifically, as they all have their electronic shells completed, the material is magnetic. This shows that what matters is their Fermi surface, instead of their local structural properties [4].

Both descriptions can be derived from the Hubbard Model. In the itinerant case, a simple one band model and a mean field approximation provide a qualitative explanation for the system magnetic properties in the limit of weak interactions. In the opposite limit, the one of strong interactions, the Hubbard Hamiltonian is reduced to a Heisenberg Hamiltonian. This model offers a good description of the magnetism of insulators.

$$\hat{\mathcal{H}}_{Stoner} = \sum_{\vec{\kappa},\sigma} \left(\varepsilon_{\vec{\kappa}} + I \langle n_{-\sigma} \rangle \right) \hat{c}_{\vec{\kappa},\sigma}^\dagger \hat{c}_{\vec{\kappa},\sigma} \tag{1.2}$$

$$\hat{\mathcal{H}}_{Heisenberg} = -\sum_{i,j} J_{ij} \hat{\mathbf{S}}_i \cdot \hat{\mathbf{S}}_j \tag{1.3}$$

where $\varepsilon_{\vec{\kappa}}$ is the energy band, I is a Stoner interatomic exchange, $\langle n_{-\sigma} \rangle$ is the mean value of the number operator, J_{ij} is the exchange integral and $\hat{\mathbf{S}}_i$ is the spin vector operator.

However, materials that strictly belong to one of these groups are rare, while the great majority shows contributions of both types of magnetism, such as the itinerant magnets RFe$_4$Sb$_{12}$ ($R = Na, K, Ca, Sr, Ba$), where the Fe local electronic structure changes depending on R, being ferromagnetic ($R = Na, K$) or non-ferromagnetic ($R = Ca, Sr, Ba$) [14].

In between these two extreme limits, one can solve the Hubbard model (Eq. 1.1) by a mean-field Hartree-Fock approximation. The minimization of the total energy of the ground state wave of the N-electron system allows the calculation of whole phase diagram of the problem. The result is in Fig. 1.1 for a 2D electronic system (in 1D a there aren't long-range orders due to the quantum fluctuations, even in the ground state [11]). The Hartree-Fock approximation provides only a qualitative scenario for the diversity of phases that can merge form the Hubbard model. The phase diagram in Fig. 1.1 give an idea of the complexity of the problem even in this simple approximation,
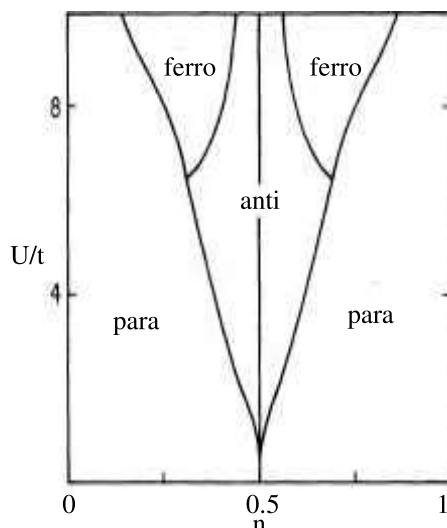
Fig. 1.1: Phase diagram for the ground state of the 2D Hubbard Model with a mean-field approximation at the strong coupling limit, as a function of *U/t* and the electronic filling *n*. Phases represented are paramagnetic (para), ferromagnetic (ferro), antiferromagnetic (anti). Note that for the case of half filling ($n = 0.5$), although quite unstable/sensitive for large electronic delocalization (large *t*), the ground state *always* displays an antiferromagnetic long-range ordering. Adapted from [15].

From the Fig. 1.1 it is clear that it is possible for many ordered ground-state phases to exist, competing or cooperating between themselves, showing how rich is the physics of the Hubbard model. Others ground states can be encountered for different approximations, or extra terms in the Hamiltonian (such as electron-phonon interactions). Among these we can find *charge density wave* (CDW), *spin density wave* (SDW) and *superconductivity* (SC).

CDW and SDW are spatial modulations of the electronic charge and electronic spins, respectively. Both transitions are accompanied by lattice distortions. For the later, this is a very small effect, while it is a large effect for the former (Fig. 1.2). SDW further requires electron-electron interactions [18]. Moreover, they still can coexist [19].
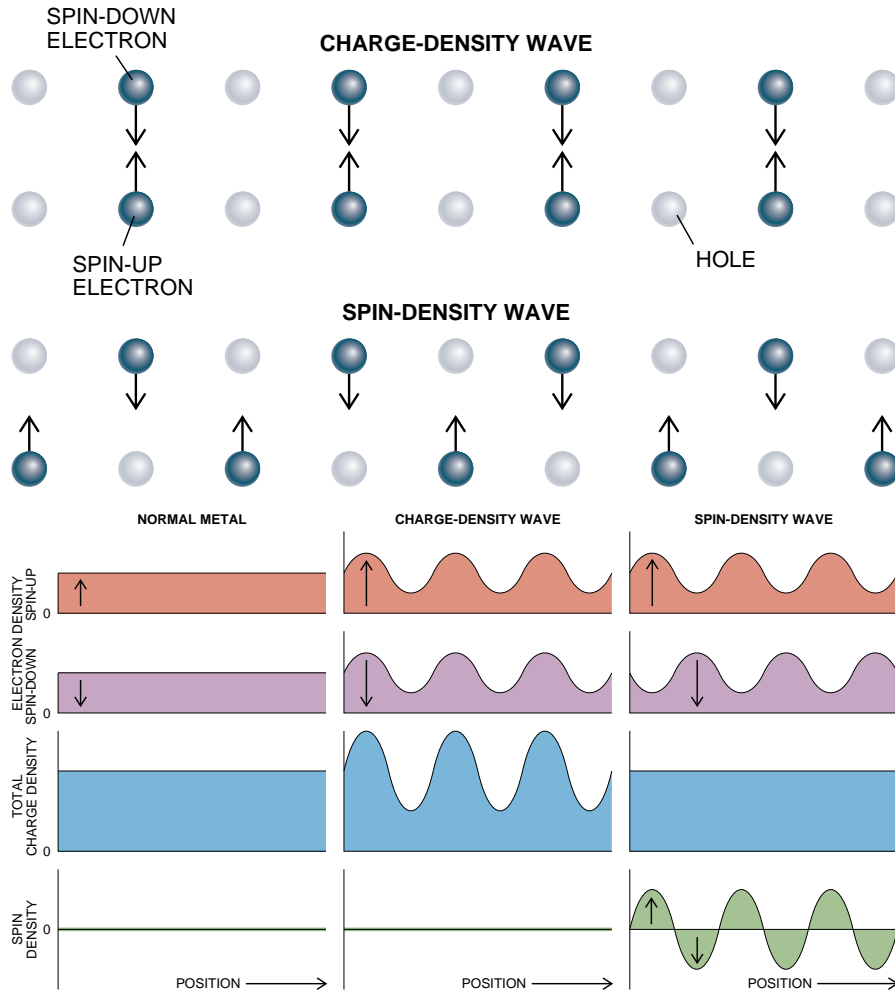
Fig. 1.2: Schematic view of CDW and SDW. Note that for the *charge density wave*, the charge and both the spins up and down densities have the same phase and periodicity, while for the *spin density wave* the charge density is constant, and the spins up and down densities have the same periodicity with different phases. Reprinted from [17].

As for SC, which is a really broad field of study, at this first moment we will give a glance over *conventional SC*. This phase is formed by electron pairs (called Cooper pairs) through an effective attractive electron-phonon interaction. The formation of the Cooper pairs opens a superconducting gap in the band structure, lowering the ground state energy [20, 26]. This theory is called BCS, and was proposed in 1957 by John Bardeen, Leon N Cooper and Robert Schrieffer, for which they were awarded the Nobel Prize in Physics in 1972 [27].

Superconductors have many properties of interest, first documented by Heike Kamerlingh Onnes in 1911 (for which he received a Nobel Prize in Physics in 1913), when he found out that the resistance of mercury dropped from 0.1Ω to less than $10^{-6}\Omega$ within $0.1K$, at $4.20K$ [21]. This phenomenon virtually allows electric current to flow without dissipation in the superconducting material. Later it was discovered that magnetic fields were repelled from within a superconductor, which is known as the Meissner effect [22].

In terms of magnetic field penetration, superconductors are classified into type I and II

superconductors (Fig. 1.3). Type I superconductors expels the external magnetic field until it is strong enough to reach H_c, destroying the superconducting state afterwards. The second type has two critical points for the external field, H_{c1} and H_{c2}; until it hits the first, the material behaves like a type I superconductor. For $H > H_{c1}$, vortices (magnetic flux quantum) emerge on the superconductor surface, destroying superconductivity only locally, allowing the external field to partially penetrate. If H reaches H_{c2}, then the superconducting state is completely destroyed [23, 26].

If the magnetic field is strong and the material is thin enough, it can pass through the whole material. This leads to quantum lock-in, where the superconductor is spatially trapped inside the magnetic field, not being able to move without an outside force.
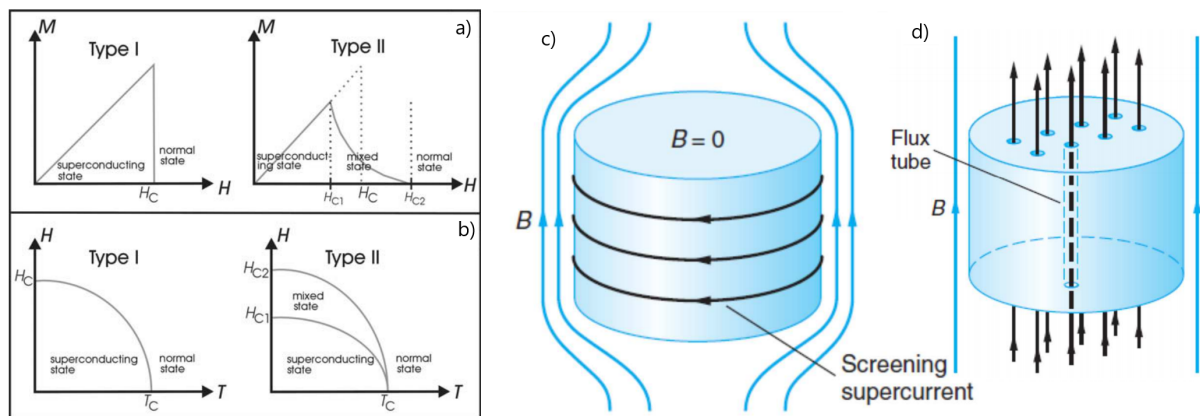
Fig. 1.3: (a) Type I and (b) II SC behaviours under magnetic field and temperature. (c) Meissner effect, where supercurrents on the surface of the material creates an internal magnetic field to nullify the external magntic field that penetrates. (d) Quantum locking in type II SC. Reprinted from [24, 26].

Although most materials need to be cooled down to extreme low temperatures to become superconductors, after their discovery people all around the world were trying to find the so called high-T_c superconductor [28]. It wasn't until 1986 that the first was obtained, a lanthanum-based cuprate perovskite with $T_c = 35K$, by J. Georg Bednorz and K. Alex Müller (Nobel Prize in Physics in 1987). This discovery mark the beginning of the *cuprate* family of high temperature superconductor materials [2, 30, 31].

Many other families were discovered through the years, with T_c reaching up to 203K [29], all of them having many representatives (Fig. 1.4). Apart from having high-T_c they also draw attention because most of them can't be understood under the BCS theory, hence receiving the name *unconventional superconductors*. In this type of superconductor, the superconducting state is still related to the condensation of Cooper pairs, but the pairs are not formed via phonons, but rather by other mechanisms. An important mechanism of that spin fluctuations to a magnetic phase near the superconducting phase [32, 35].
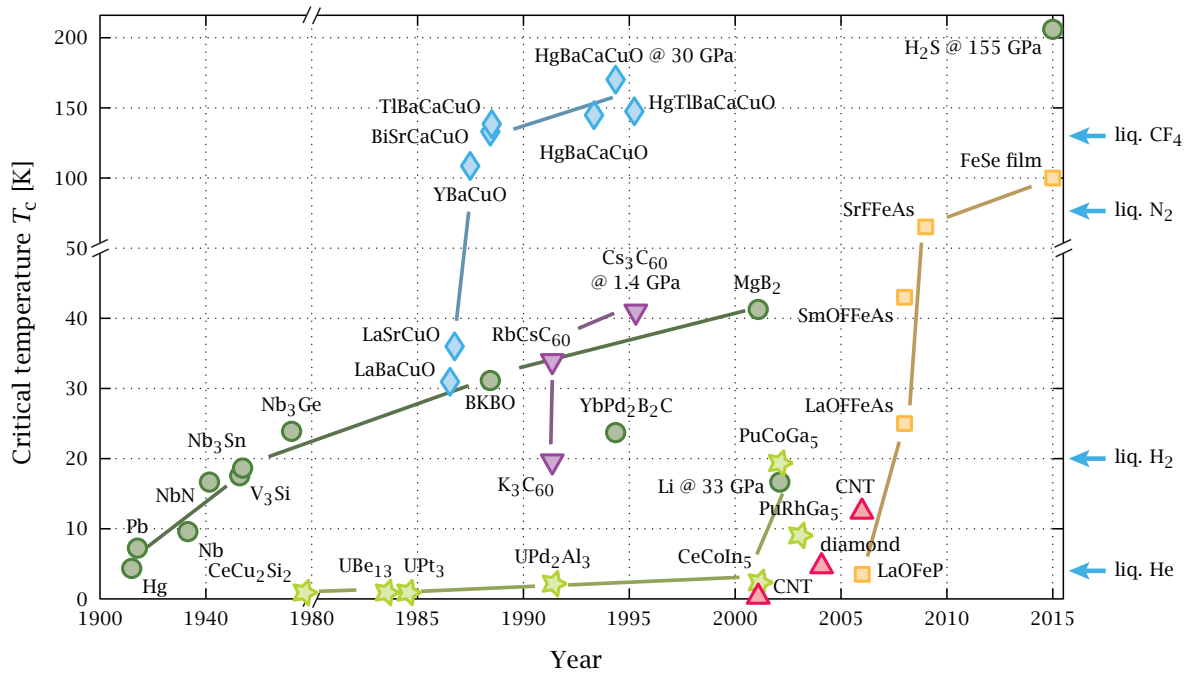
Fig. 1.4: Timeline of the discovery of superconductors since 1911 with their respective critical temperatures and families. The latter represented by colors: BCS (dark green circle), Heavy-fermions (light green star), Cuprate (blue diamond), fullerenes (purple inverted triangle), Carbon-allotrope (red triangle) and Iron-based (orange square). For reference, on the right we have the temperatures for liquids CF_4, N_2, H_2 and He, commonly used as cooling agents. Reprinted from [28].

One of the main differences between conventional and unconventional superconductors concerns the superconducting gap symmetry. In the former, Cooper pairs are in relative zero angular momentum state, leading to *s-wave pairing*. Here, the gap is isotropic over the whole Fermi surface. In the later, the Cooper pairs interact via a pairing potential with non-zero angular momentum. In this case, the gap can be anisotropic over the momentum space. In this sign change occurs in a region of momentum space that coincides with the material Fermi surface, this means that they must be zero in the border between the opposite sign, which defines a *noda reagion* (can be a point, a line or a surface). Thus, the SC state may be not fully gapped in a unconventional superconductor. An important example is the $2\hbar$ (*d-wave pairing*) in cuprates.

There is as well the case of extended s-wave pairing. In this scenario one can have the $s^{++(--)}$ for only positive (negative) gap, s^{+-} for both not intersecting, and nodal s^{+-} if they do. As in the case of d-wave, superconductors described by this extended s-wave pairing scenario may present a noded gap. More complex gap symmetries are possible in multiband systems, $s + is$ for example, which breaks time-reversal symmetry by phase differences which are not integer multiples of π [33, 34, 45].

Unconventional SC includes, but is not limited to, the already cited cuprates, fullerenes, discovered in 1991 [38, 39, 40], heavy-fermions in 1978 [35, 36, 37] and iron-based in 2006 [41, 42, 43].

The latter, also known as *Iron Based Superconductors* (IBS or FeSC), includes a group called iron arsenide materials. Discovered in 2008 [44], they are a landmark on the run for a room temperature SC, as most of the previous unconventional superconductors were cuprates. FeSCs are formed by conducting layers of iron and pnictides (group 15 of the periodic table, usually As or P) in-between layers of other elements (called the spacer or charge reservoir block [46]). FeSCs are divided in families, based on their stoichiometric (Fig. 1.5), we have as examples the *1111* (*R*FeAsO, *R* as rare earth) [42, 43, 47], *111* (*A*FeAs, *A* as alkali metal) [48, 49, 50] and *122* (*Ae*Fe$_2$*Pn*$_2$, *Ae* as alkaline-earth metal, *Pn* as pnictide) [51, 52, 53].
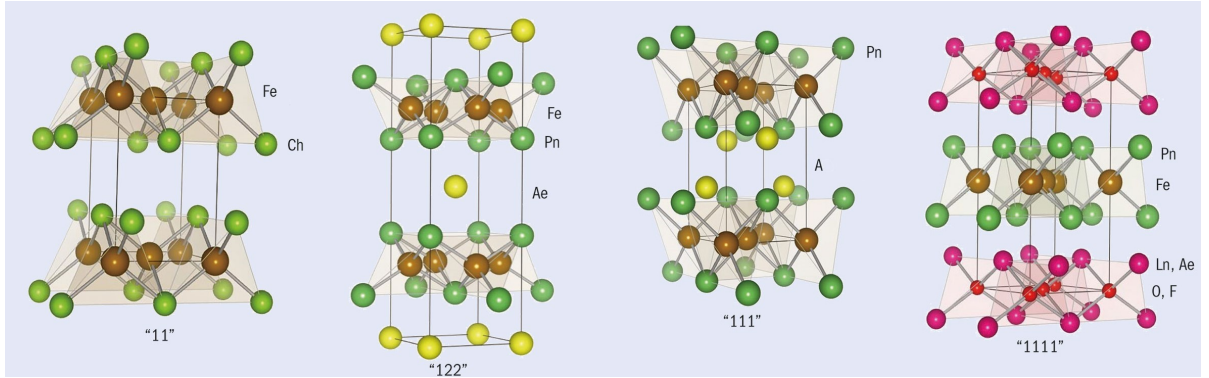
Fig. 1.5: Crystal structures of four "families" of iron-based superconductors, showing the positions of iron atoms (brown), pnictogen atoms (green, labelled Pn) and chalcogen atoms (green, labelled Ch) in each family. The positions of alkali atoms (A), alkaline-earth atoms (Ae) and other elements present in the "111", "122" and "1111" families are also shown. Reprinted from [45].

All of them have a common feature that is the tetrahedral coordination of the iron atoms by the *Pn* atoms. This coordination can be treated as a tetrahedral-like crystal-field, that breaks the *3d* orbitals degeneracy of the Fe central atom into two groups, t_{2g} (orbitals d_{xy}, d_{xz} and d_{yz}) and e_g (orbitals $d_{x^2-y^2}$ and d_{z^2}), which can be seen in Fig. 1.6. This lifting of the *3d* degeneracy make each orbital to contribute differently to the Fermi surface [54, 55]. Therefore, the FeScs Fermi surface has a strong orbital character.
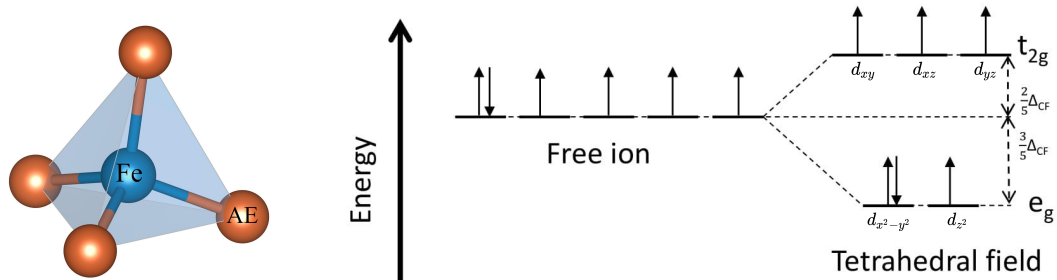
Fig. 1.6: (Left) tetrahedral coordination of the alkaline-earth atoms *AE* around the Fe atom, image made with VESTA [56], and (right) crystal-field splitting for a tetrahedral field on the *3d*^{6} orbitals of Fe^{+2} (high-spin configuration), where Δ_{CF} is the resultant total energy split.

In this way, one can deduce that the local properties of the tetrahedron are connected to the Fermi surface properties. This incites the question as to what happens if one perturbs this tetrahedral coordination in different ways. The answer is that we can drastically change the system macroscopic properties, be chemical substitution at different crystallographic sites in the material crystal structure, or even by applying pressure [57, 58, 59, 60, 61, 62, 63], as Fig. 1.7 shows.

Chemical substitution effects are very diverse. In may include charge doping, local distortions of the Fe coordination, chemical pressure, etc... all of which can tune the material electronic phase diagrama to a distinct phase.
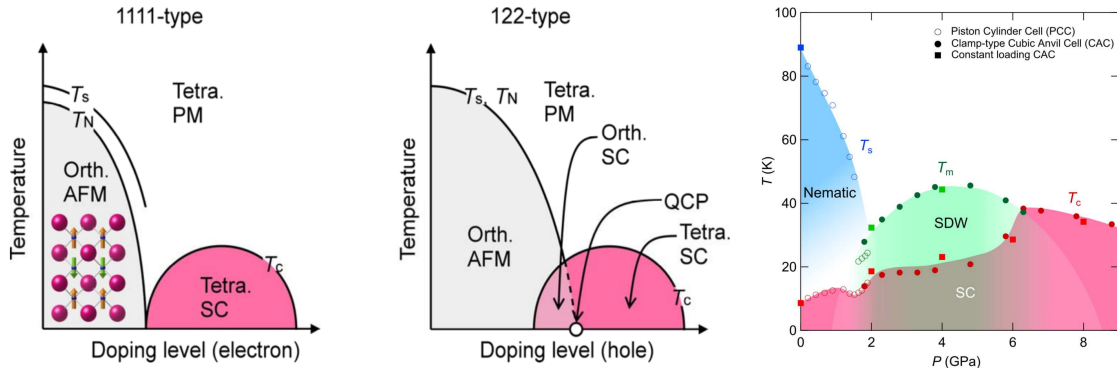
Fig. 1.7: (Left) Phase diagram of 1111 family for electron doping, (middle) 122 family with hole doping [61]. (Right) phase diagram for FeSe by pressure [62]. Phases: T_s for structural transition temperature, T_N for Néel temperature (antiferromagnetic below and paramagnetic above it), *PM* for Pauli paramagnetism, *Orth. AFM* for antiferromagnetic orthogonal structure phase, *Tetra.* for tegragonal structure phase, T_c for SC phase, *QCP* for quantrum critical point [64], T_m for magnetic transition temperature.

In fact, the connection between pressure and doping (chemical pressure) was first experimentally explored by Kimber et al. [65], followed by Johannes et al. [66] first principle calculations, leading to an interpretation where the As-Fe bond lengths and local Fe magnetic moments have a direct relationship. Soon after, Granado et al. [67] and Balédent et al. [58] have also shown similarities in both approaches to suppress the magnetic phase and the rise of a superconducting state. All of these studies were performed on the "122" compound $BaFe_2As_2$ and its doped variants, with the last two using XAS at As and Fe K edges, respectively.

As the field of research grew, an important question about the iron arsenides emerged, which concerns its electronic correlation. Understanding if the material is weakly or strongly correlated is decisive to develop a model capable of explaining electronic properties of already known materials, as well to predict new ones, not to mention the need for a quantitative model. Whether which of regime rules is still a debate, with theoretical and experimental studies pointing towards either a localized [71], itinerant [72] or even both [73] descriptions, suggesting that these compounds are indeed in the border between weak and strong correlations [74, 75, 76, 77, 78].

To figure this out we first need to acknowledge the multi-orbital nature of the IBSs electronic states. Focusing on the "122" compounds $SrFe_2As_2$ and $BaFe_2As_2$, the electronic structure of these material was investigated looking at near edge region of XAS spectra (XANES) by XAS experiments. The first relavant piece of finding of this type of experiments, was obtained from Fe K edge experiments. Here, the Fe valence was shown to be robustly +2, under Co doping, pressure or temperature [57, 58, 59, 60]. This constant valence means that there are 6 electrons distributed over the five iron 3d orbitals, and by applying a five-orbital or even three-orbital (d_{xy}, d_{xz}, d_{yz}) Hubbard model we can have different values for the Hubbard interaction U and Hunds coupling J for each orbital. This leads to a distinct orbital selective behaviour. For instance, some these orbitals can display stronger electronic correlations, that will lead to Mott localization, or to an *orbital-selective Mott phase* (OSMP), since not all orbitals will display such strong electronic correlation. The orbital-selective Mott phase is observed when one can see the localization of one specific orbital, while others remain itinerant [79, 80]. This is supported by angle resolved photoemission spectroscopy (ARPES) experiments [80, 81], Hall [82] and high-pressure transport measurements [83], as well by terahertz [84] and pump-probe [85] spectroscopy.

We could also reach a Mott phase on $Ba(Fe_{1-x}Cr_x)_2As_2$ or $Ba_{1-x}K_xFe_2As_2$ [86], where the compound is being doped by holes. This would push the Fe $3d$ electronic filling in $BaFe_2As_2$ closer to 5 electrons, which is a half filling regime [76, 87, 88], where a Mott phase could be realized. In [86], XAS and X-ray emission spectroscopy (XES) experiment could provide evidence for this type of physics. We should point out, however, that this is not the only possible interpretation to their results. In particular, one should keep in mind that, so far, no clear and direct evidence that the Fe electronic filling changes in the IBS phase diagram was found.

Indeed, the Fe valence is quitte rigid in the IBS phase diagram. This rigidness of the Fe as a fucntion of doping is suggested to be due As $4p$ orbitals acting like a charge sink. This effect was probed by As K edge XAS [60, 89] exemperiments. Balédent *et al*, has shown that either by pressure or chemical pressure, an increase on the mixing of Fe 3d and As 4p orbitals takes place, and the charge transfer caused by Co seems to go to As orbitals. The whole effect draw attention to the key role that As derived orbitals play on the electronic properties of the iron pnictides [89].

To grasp a better understanding about what drives the system towards higher T_c, many studies were made regarding the correlation between T_c and different parameters, with a focus on the properties of the Fe tetrahedron (Fig. 1.8). The relation between T_c and the bond angle α of the Pn(Ch)-Fe-Pn(Ch) bond, the anion height h_{Pn} in the Fe layer and the distance between the Fe layers, were investigated by a number of experiments [68, 69, 70, 74]. In particular, Lee *et al* has shown that, in general, the closer the tetrahedron is to be perfect ($\alpha = 109.47°$), the higher the critical temperature is [70]. Despite such parameters being found and attempted to be correlated to the T_c, none of them can be treated as rules, as they have discrepancies. As example, we have the 11-type compound $FeSe_{1-x}Te_x$ not contemplated by both the bond angle

α and the anion height h_{Pn} hypothesis. For the distance between the Fe layers, no correlation with T_c was seen.

Explorations more focused on the FS properties were also performed [33, 90, 91]. The results corroborate the idea that the phases are indeed very sensitive to electronic doping, also showing how the individual *3d* orbitals contribute to the FS in a distinguished manner (Fig. 1.9).
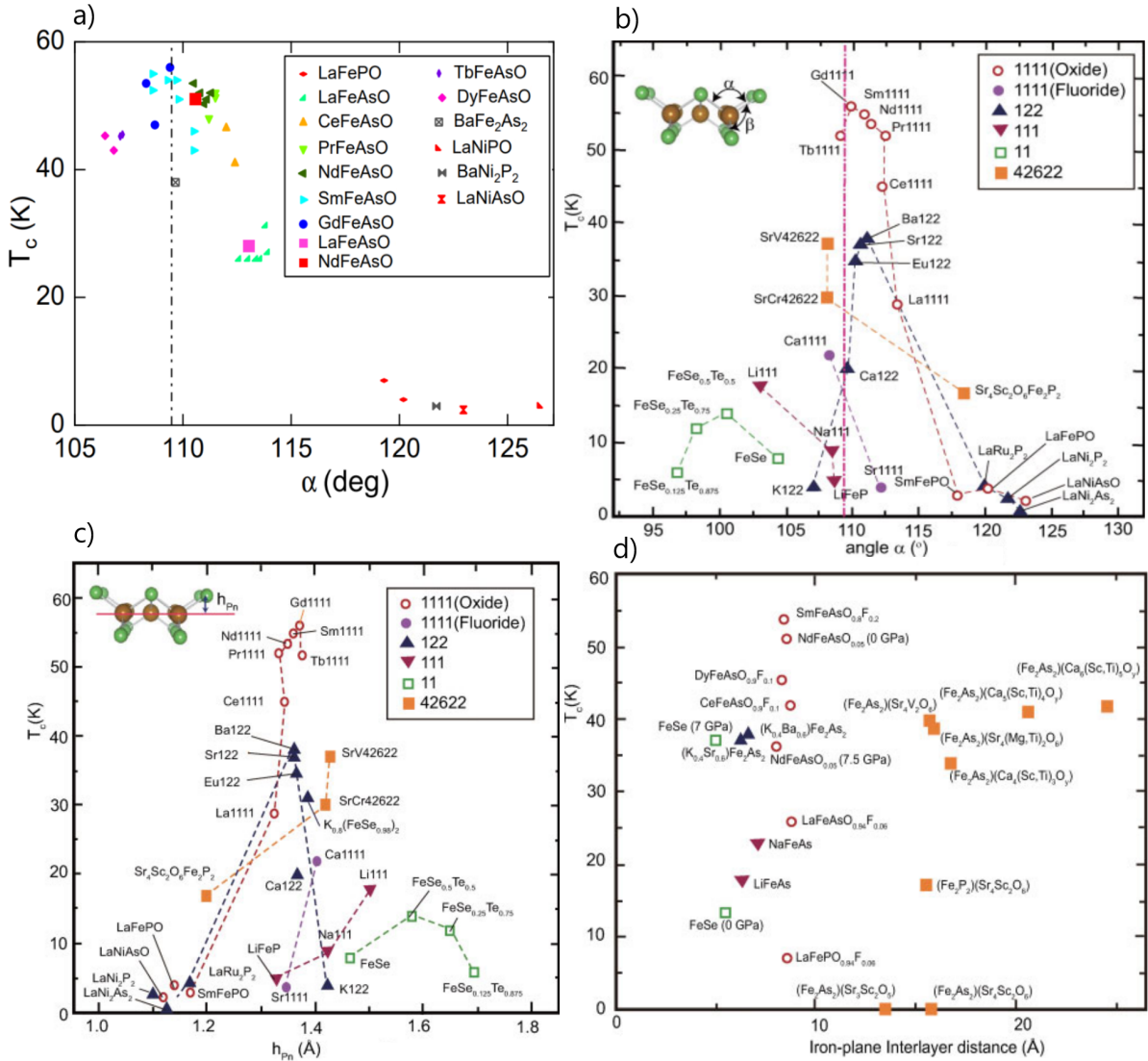
Fig. 1.8: Different IBS families T_c dependence over a-b) Pn(Ch)-Fe-Pn(Ch) bond angle, c) Pn height from the Fe layer and d) distance between the Fe layers. In a-b) the angle α is measured from the compound near room temperature, where we can see that the T_c peaks when this angle is nearest to be 109.47° (represented by the vertical dashed lines), which means a a regular tetrahedron. In c) the distance h_{Pn} is also measured from the compound at room temperature, showing a tendency for higher T_c near the 1.4 value. d) shows no consistency with the distance between the Fe layers. Adapted from [69, 70].
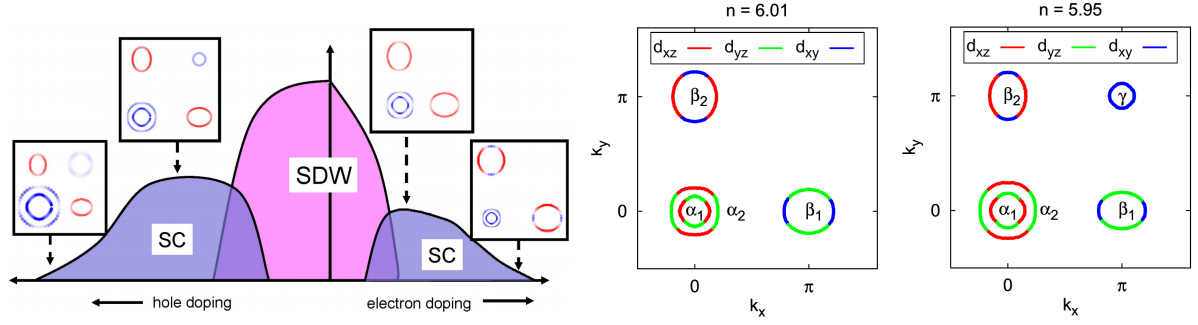
Fig. 1.9: (Left) Schematic phase diagram of Fe-based superconductors vs. doping, with order parameter expected from 2D spin fluctuation theory plotted in one quadrant of the Brillouin zone as color on Fermi surface [red=+,blue=-]. (Center and right) DFT calculations for LaFeAsO, Fermi sheets of the five-band model for the electron filling n = 6.01 and 5.95 with colors indicating majority orbital character. The γ Fermi surface sheet is a hole pocket that appears for $\sim$1% hole doping. Reprinted from [33, 90].

In the present work, we are going to investigate the role of the extra electrons/holes in the system by performing polarization dependent X-ray Absorption Spectroscopy (XAS) experiments, probing the Fe and As K edge of the 122-type parent compound $BaFe_2As_2$ and its doped variants.

At room temperature and ambient pressure, our parent compound, the 122 iron pnictide $BaFe_2As_2$, is a semimetal, with a tetragonal lattice (space group I4/mmm) and Pauli paramagnet. Resistivity and susceptibility Measurements show an electronic decoupling between the different Fe layers, meaning the material is *quasi* 2D [92]. Its ground state changes to an itinerant antiferromagnetic phase, a SDW, at T_N = 134K, and we can go even further, destabilizing it by electronic doping or applying pressure, forcing a SC state (Fig. 1.10).

An interesting feature is that the phase diagram is not symmetric under electronic doping for transition metal substitution. Specifically, from Fig. 1.10 we can see that by doping either with electrons (Co in the Fe site) or holes (K in the Ba site) we can get to this new state (which can also be achieved by electron doping on the Fe site through Ni, Cu, Rh, Pd, Au [93, 94, 95, 96]). However, if we dope again with holes (via Mn, Cr or V), but this time at the Fe site, superconductivity is not found [97, 98, 99, 100]. This observation calls into question the specific effects implied by chemical substitution. If the transitions metals are indeed doping the material, in the sense of transferring of charge, why is that some substitutions do not lead to a superconducting state? In turn, this supports the idea that when doping at the Fe site, the disruption in the tetrahedron electronic/structural properties is the key parameter to understand the phase diagram of the IBS. Therefore, "doping" is an umbrella term that encompass a broad set of physical/chemical effects. We shall keep using this term, but one should in mind this restriction.
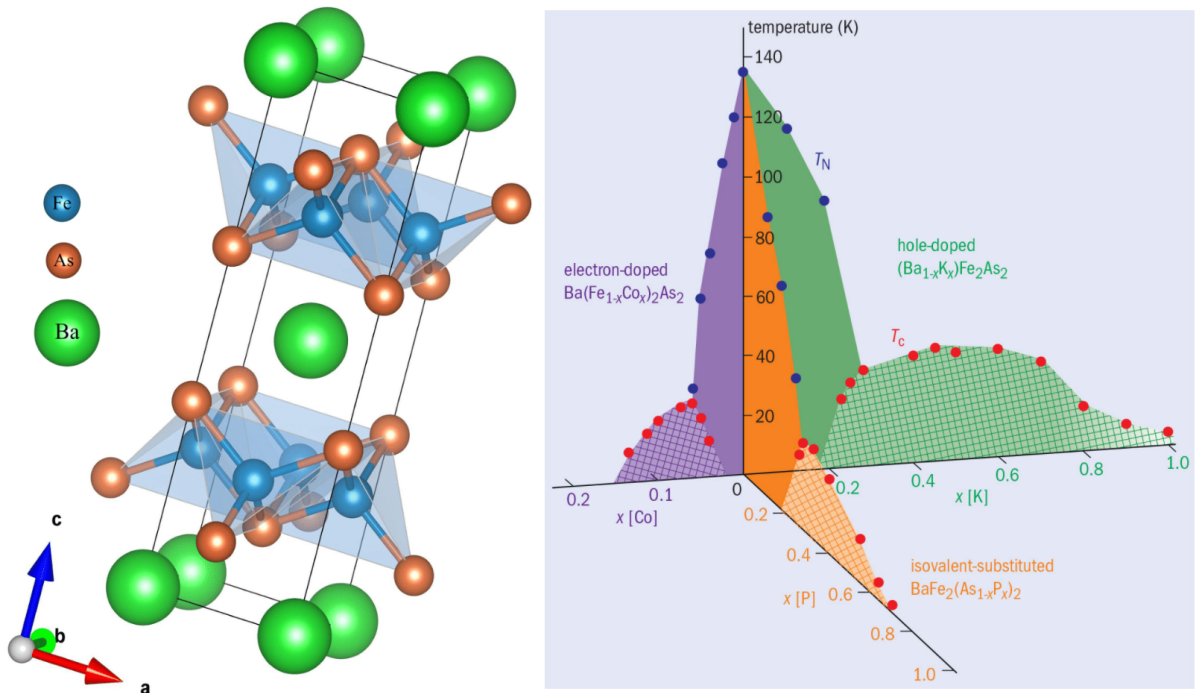
Fig. 1.10: (Left) Crystal structure of $BaFe_2As_2$ made with VESTA [56]. Blue for iron (Fe), orange for arsenic (As) and green for barium (Phase diagram of $BaFe_2As_2$ for electron doping via Co (purple, left), hole doping via K (green, right) and isovalent doping via P (orange, middle). Dashed and filled regions for the SC and SDW phases, respectively, reprinted from [45].

DFT calculations and ARPES measurements at this specific material were also performed, highlighting the role of the different iron $3d$ orbitals for the FS, above and below the antiferromagnetic (AFM) phase [91, 101, 102]. Although how much each orbital contributes to the FS has changed over the years, all models supports the multiband character.

Having the multiband character paired with the different d orbitals symmetries, polarized X-ray Absorption Spectroscopy (XAS) can be a good probe to understand how electronic doping acts over the tetrahedron properties.

Chapter 2

Materials and Methods

The samples investigated in this work were obtained in collaboration. Single crystals of the parent compound $BaFe_2As_2$ and the Mn and Co substituted materials $Ba(Fe_{1-x}M_x)_2As_2$ (x = 0.08 and M = Co or Mn) were selected for the experiments, which were performed at room temperature.

The samples were synthesized and characterized by T. M. Garitezi *et al.* [103]. Single crystals were grown by a metallic In-flux technique, heat treated with temperatures as high as 1150°C for as long as 21 hours, depending on the dopant. Characterization included x-ray powder diffraction, elemental analysis using a commercial energy dispersive spectroscopy (EDS) microprobe, electrical resistivity (via PPMS), magnetic susceptibilities (with SQUID) and NMR measurements [103]. Samples didn't show evidence of flux incorporation and were of extremely high quality, with the expected lattice parameters and T_c.
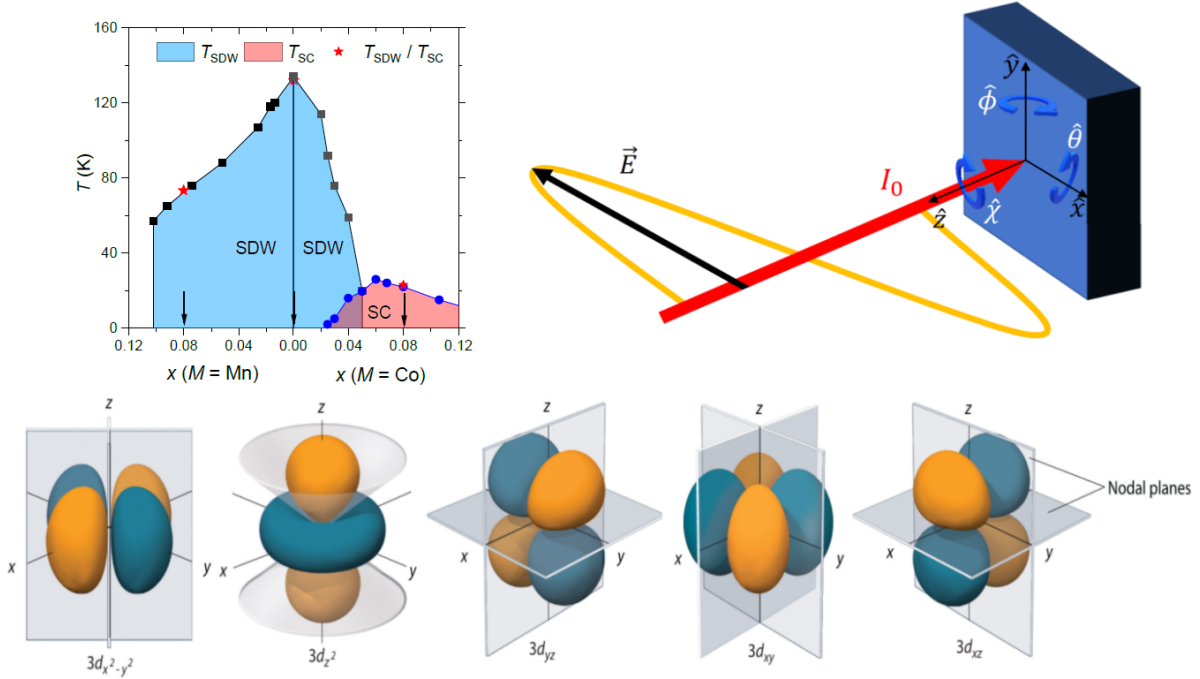
Fig. 2.1: (Top left) Phase diagram of $Ba(Fe_{2-x}M_x)As_2$ (M = Mn, Co) for our chosen samples. (Top right) Schematic experimental setup, showing the alignment of the sample (blue), beam (red) and its polarization direction (yellow), as well as the rotations around each axis. (Bottom) d orbitals symmetries, adapted from [104].

The polarization dependence of the XAS spectra was investigated by rotating the samples. The rotations axis x, y and z are defined in figure Fig. 2.1, and their respective rotation angles are θ, ϕ and χ. With this type of experiment we are able to distinguish the distribution of the density of unoccupied states in real space of the hybrid bands formed by d orbitals and p orbitals. Indeed, the dipole selection rules dominate the intensity of all spectral absorption features, and therefore d orbitals are probed in a indirect manner, via their hybridization with p orbitals (Fig. 2.1).

2.1 Polarized X-ray Absorption Spectroscopy (XAS)

While studying the interaction between x-rays and matter we can face many different effects, one of them being x-ray absorption. This phenomenon can be empirically described by Lambert-Beer law, which states that if we have an initial beam of intensity I_0 going through a material of thickness x, the beam at the end will have its intensity reduced by $e^{-\mu x}$ (Fig. 2.2).

$$I(x) = I_0 e^{-\mu x} \qquad (2.1)$$

$$\mu = \eta \sigma_{total} \qquad (2.2)$$

The attenuation coefficient μ can be understood as how hard it is for each photon to pass through the material, being directly proportional to the so called cross section σ_{total} and to the

material's atoms density η. The total cross section reflects the probability of a photon to interact with the material's atoms, either by scattering or absorption. [105, 106, 107].
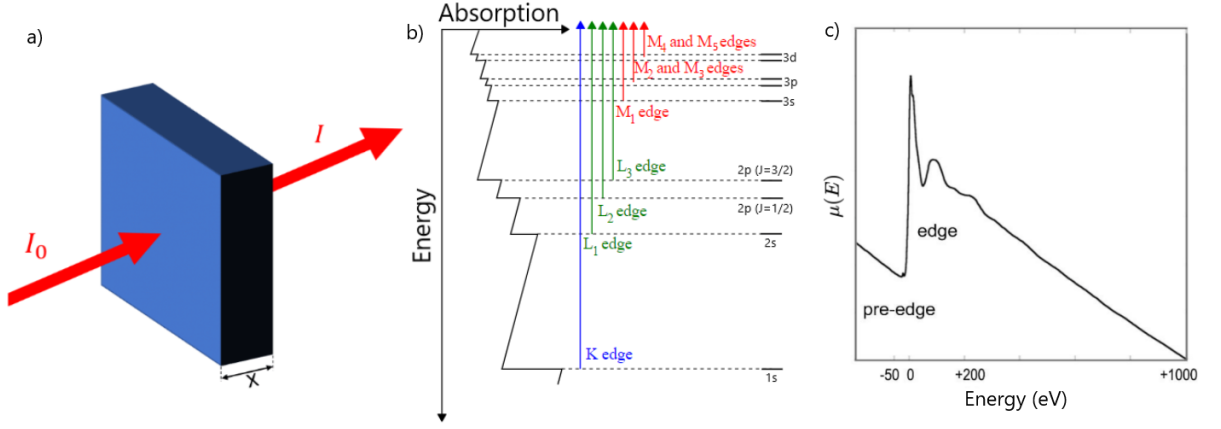
Fig. 2.2: a) Schematic view of an incident beam I_0 going through a material of thickness x and the exiting beam I of weaker intensity. b) Schematic view of transitions from K, L and M edges, as well with their respective qualitative absorption coefficients. Adapted from [108] c) Generic example of an edge being probed by x-rays (XAS spectrum). Adapted from [109].

We can correlate the absorption cross section σ_a to the first-order transition probability per unit time T_{if}, from a initial state i to a final state f, divided by the incident photon flux. It was derived by Paul Dirac and then called by Enrico Fermi the *Golden Rule No. 2* (the Golden Rule No.1 refers to the second-order term, which describe scattering processes).

$$T_{if} = \frac{2\pi}{\hbar} \left| \langle f | \mathcal{H}_{int} | i \rangle + \sum_n \frac{\langle f | \mathcal{H}_{int} | n \rangle \langle n | \mathcal{H}_{int} | i \rangle}{\varepsilon_i - \varepsilon_n} \right|^2 \delta(\varepsilon_i - \varepsilon_f) \rho(\varepsilon_f) \qquad (2.3)$$

where $\mathcal{H}_{int}$ is the interaction Hamiltonian, the sum is over all the possible states of energy ε_n and $\rho(\varepsilon_f)$ is the final state density.

For a qualitative approach we can omit the second-order term. The interaction Hamiltonian is approximated as the coupling of the momentum operator **p** with the vector potential **A**, which comes about from the kinetic energy term because of the transformation of the canonical momentum for a particle in an electromagnetic field. We treat the field degrees of freedom in second quantized form and apply the electric dipole approximation to calculate the matrix elements. This leaves us with:

$$\sigma_a = 4\pi^2 \alpha_f \hbar\omega |\langle f | \boldsymbol{\epsilon} \cdot \boldsymbol{r} | i \rangle|^2 \delta[\hbar\omega - (E_f - E_i)] \rho(E_f) \qquad , \qquad \alpha_f = \frac{e^2}{4\pi\epsilon_0 \hbar c} \qquad (2.4)$$

By integrating the absorption cross section σ_a over a certain energy range, we get the XAS resonance intensity I_{res}, which explicitly shows the XAS intensity dependency on the polarization dependent dipole operator P_α^q, where α is the polarization component in the x, y and z axis, and q is the photon angular momentum, being 0 for linear polarization or ± 1 for circular

polarization.

$$I_{res} = 4\pi^2 \alpha_f \hbar\omega |\langle f| P_\alpha^q |i\rangle|^2 \qquad , \qquad P_\alpha^q = \boldsymbol{\epsilon} \cdot \boldsymbol{r} \qquad (2.5)$$

Taking the terms with linear polarization and rewriting them in terms of the spherical harmonics $Y_{lm}(\theta, \phi)$, we can now translate the polarization components in the x, y and z directions to our experimental angles χ, ϕ and θ, taking into account that our beam default polarization is on the x direction (the reason behind this will be shown later).

$$E \parallel \hat{x} \rightarrow P_x^0 = r\sqrt{\frac{2\pi}{3}}(Y_{1,-1} - Y_{1,1})$$

$$P_\chi = \cos\chi P_x^0 + \sin\chi P_y^0$$

$$E \parallel \hat{y} \rightarrow P_y^0 = r\sqrt{\frac{2\pi}{3}}(Y_{1,-1} + Y_{1,1}) \quad (2.6)$$

$$P_\phi = \cos\phi P_x^0 + \sin\phi P_z^0 \qquad (2.7)$$

$$E \parallel \hat{z} \rightarrow P_z^0 = r\sqrt{\frac{4\pi}{3}}(Y_{1,0})$$

$$P_\theta = P_x^0$$

2.1.1 X-ray Absorption Near Edge Structure (XANES) in BaFe$_2$As$_2$

From Eq. 2.4 it is clear that the absorption cross section σ_a is greater when the incident photon energy is closer to the energy for freeing an electron and creating a vacancy. This set of specific energies is called absorption edges. Each edge is named after the type of electronic shell from which the electron is being excited. For example, the Fe K-edge at ∼7112 keV, denote the excitation of the innermost *1s* core electron, and the Fe L$_1$-edge at ∼0.846 keV from the *2s* shell. Every excitation process allows another bound electron, in a higher energy state, to decay and occupy the low lying empty state (this transition must obey certain selection rules, such as the dipole one).

Overall, the absorption spectra can be split up in two main regions, the *X-ray Absorption Near Edge Structure* (*XANES*) and the *Extended X-ray Absorption Fine Structure* (*EXAFS*), each having their own characteristics. The first one, XANES, ranges only few eV below and above the edge energy, sometimes displaying a pre-edge and then a rising edge, where the absorption sharply increases due to the incident photon energy matching the edge energy and ionizing core electrons, the main electronic transition. The second, EXAFS, has an oscillatory nature which persists over several hundreds of eV over the edge energy, called the Kronig structure. It is caused by constructive and destructive interferences between the previously unbounded electrons, the photoelectrons, being scattered through the material (Fig. 2.3).

Each of these two distinct regions give us different information about the material. The central metal oxidation state, coordination number of the central atom, bond angle are examples of parameters determined by XANES. The interatomic distances, near neighbor coordination numbers and lattice dynamics are examples of paramters determined by EXAFS [110, 111, 112, 113, 114].

In transition metals, the $3d$ levels are not completely filled their K-edge spectra usually display a the pre-edge structure. This can be allowed by quadrupolar transitions, but that is usually a weak effect. Additionally, there could be contributions due to crystal field and ligand field in transition metal coordination complexes. The ligand orbitals can hybridize (*s* and *p* orbitals into sp^3 orbitals) and then mix with the metal orbitals. This metal-ligand pd mixing allow dipole transitions with a significant intensity. Each combination of crystal field and orbitals will lead to different *molecular orbitals*, the net orbital energy levels for a compound. To catch a glimpse on how this develops, we will need to introduce crystal field, point group and ligand field theories [54].
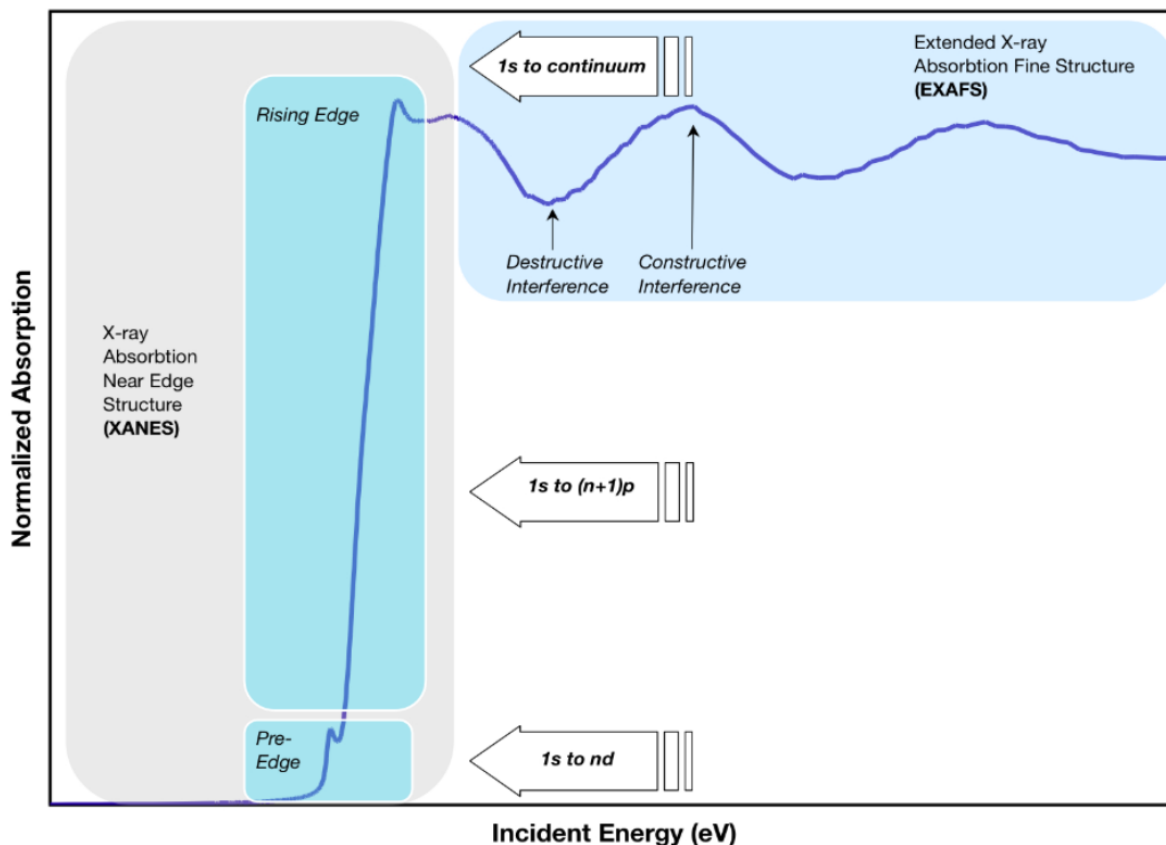
Fig. 2.3: Example of a XAS spectrum, broke into the two main regions of XANES and EXAFS, and their respective features. Adapted from [110].

First, we need to know that orbitals will only mix if they have the same symmetry, so let's take the character table of the point group T_d (Fig. 2.4), the same group from the FePn tetrahedron in our parent compound BaFe$_2$As$_2$. It tell us the symmetries and representations present in this point group, then we need to find which of them better describes our orbitals (this is done by checking each representation property on each orbital). Having all the orbitals with their respective symmetries assigned, we can correctly mix them.

We can now see that the metal $3d$ orbitals indeed mix with the ligand sp^3 orbitals, leading to two reasonable thoughts: *i)* this bypass the dipole's transition rules, now allowing contributions from the $3d$ orbitals to the pre-edge region, and *ii)* the electrons from the ligands plays an important role in the compound's electronic configuration.

The first effect can be seen in multiple XAS experiments where a pre-edge with relative high intensity is found [58, 57, 60, 86, 116], which can also be supported by simulations where the intensity from dipole and quadrupole transitions were calculated separately [57, 86], settling down which type of selection rules (either dipole or quadrupole) dominate the pre-edge intensity. All experimental evidence and calculations indicate that all absorption features, including the pre-edge structure, of the Fe K edge in our materials originate from dipole transitions.

A very relevant effect of the ligand orbitals was discussed by Baledent *et al.* [89]. Using XAS at As K edge, it was shown that either by applying pressure or doping with Co, the Fe-

As bond lengths could be shorten, leading Fe 3d and As 4p orbitals to have a larger mixing. This mixing was also observed in DFT calculations, performed by the means of full-potential linearized augmented plane waves plus local orbitals method for both spin states [117].

The As atoms were seem to act as a charge sink, collecting electrons from Co doping, lowering its valence. This was concluded from the As K edge XAS spectra showing an energy shift of the As states to lower energies. [89, 60]

Fig. 2.4: (Top left) Character table of the point group T_d and (top right) symmetry types of the s, p and d orbitals and their respective representations. (Bottom) Molecular orbitals from a transition metal M and four ligands L with sp^3 hybridization in a tetrahedral coordination. We can see the tetrahedral crystal field splitting Δ_T within the red rectangle. Adapted from [115].

2.1.2   Brazilian Synchrotron Light Laboratory (LNLS)

A great portion of the techniques used to probe electronic properties of materials uses x-rays, hence a good beam is essential. One of the ways to reach this is through synchrotrons, a type of cyclic particle accelerator that uses varying magnetic fields to bend and accelerate the particles in the storage ring. By bending electric charged particles (great majority of the time they are electrons) with dipole magnets, they produce synchrotron radiation which is emitted perpendicular to the particles trajectory. Quadrupole and sextupoles magnets are used to modify

the beams cross-section.

Considering a standard procedure, these particles are first generated by an *electron gun*, go through a *linear accelerator* and then into the *booster*, a (usually smaller) synchrotron where they are accelerate to their maximum velocity. Finally they are moved to the *storage ring*, which purpose is to maintain the particles speed. On each segment where the beam is bent, synchroton radiation is emitted, thus a *beam line* can be placed there. Fine tuning of the beam for the specific experiments being held is accomplished in the beamline. Experiments are carried out at the *experiment stations*. In the straight sections of the storage ring we can find the *insertion devices* called *wigglers* and *undulators*, they are periodic structures of dipole magnets. Wigglers laterally deflect the beam creating a broad emission of synchrotron radiation, while an undulator deflection is perpendicular to the orbit plane and beam direction. Undulators produce a narrow radiation spectrum. Both types of insertion devices increase the flux and the brilliance of the radiation output. All these elementary components can be seen in the Fig. 2.5.
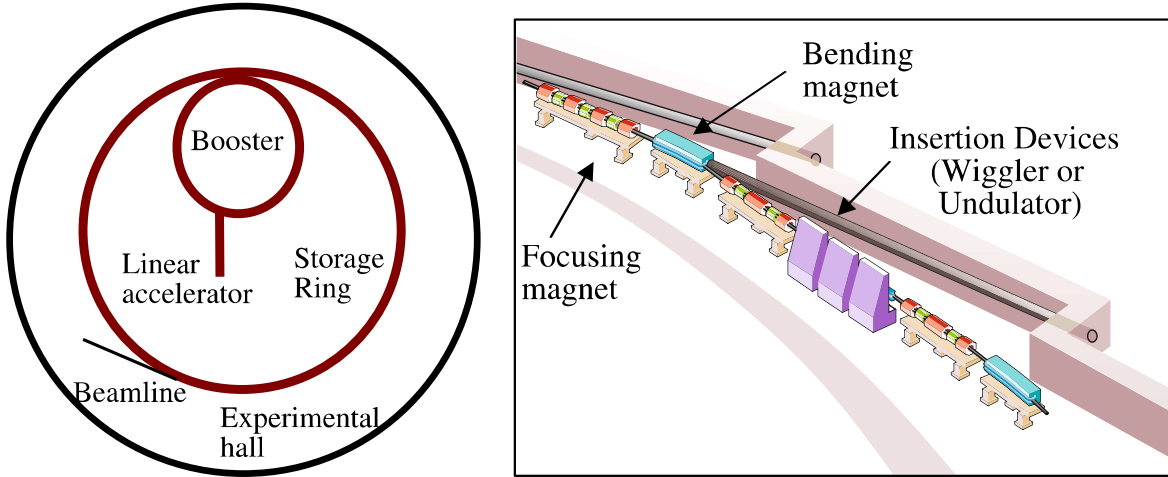
Fig. 2.5: (Left) Schematic view of the linear accelerator, booster, storage ring, beamline and experimental hall. (Right) Focusing and bending magnets, as well the insertion devices, wiggler and undulator. Reprinted from [118].

The default polarization direction in synchrotrons is in the radial direction, which means it is perpendicular to the beam while contained in the orbital plane. To see why, we first need to take the Liénard-Wiechert field equations (Eq. 2.8 and Eq. 2.9) and work them towards the relativistic generalization of Larmor's formula Eq. 2.10.

$$\mathbf{B}(\mathbf{r}, t) = -\frac{\mu_0 q}{4\pi} \left(\frac{c\,\hat{\mathbf{n}} \times \vec{\beta}}{\gamma^2 R^2 (1 - \vec{\beta} \cdot \hat{\mathbf{n}})^3} + \frac{\hat{\mathbf{n}} \times \left[\dot{\vec{\beta}} + \hat{\mathbf{n}} \times \left(\vec{\beta} \times \dot{\vec{\beta}} \right) \right]}{R(1 - \vec{\beta} \cdot \hat{\mathbf{n}})^3} \right)_{retarded} \tag{2.8}$$

$$\mathbf{E}(\mathbf{r}, t) = -\frac{q}{4\pi\varepsilon_0} \left(\frac{\hat{\mathbf{n}} - \vec{\beta}}{\gamma^2 R^2 (1 - \vec{\beta} \cdot \hat{\mathbf{n}})^3} + \frac{\hat{\mathbf{n}} \times \left[\left(\hat{\mathbf{n}} - \vec{\beta} \right) \times \dot{\vec{\beta}} \right]}{c\,R(1 - \vec{\beta} \cdot \hat{\mathbf{n}})^3} \right)_{retarded} \tag{2.9}$$

$$\frac{d^3W}{d\Omega d\omega} = \frac{q^2}{16\pi^3\varepsilon_0 c}\left|\int_{-\infty}^{\infty}\frac{\hat{\mathbf{n}}\times\left[\left(\hat{\mathbf{n}}-\vec{\beta}\right)\times\dot{\vec{\beta}}\right]}{\left(1-\hat{\mathbf{n}}\cdot\vec{\beta}\right)^2}e^{i\omega(t-\hat{\mathbf{n}}\cdot\vec{r}(t)/c)}\,dt\right|^2 \tag{2.10}$$

where $\hat{\mathbf{n}}$ is the direction from the observer to the source, $\vec{\beta}$ is the velocity of the source, γ is the Lorentz factor, R is the distance between the observer and the source, Ω is the solid angle and ω is the frequency.

Now taking the case for small angles and inputting the beam trajectory (Eq. 2.11), which for synchrotrons is a circumference, we get to Eq. 2.12, where θ is the angle between an in-plane direction and another outside it, and K is a modified Bessel function of the second kind. The $K_{2/3}^2(\xi)$ and $K_{1/3}^2(\xi)$ terms are responsible for the radiation power with a polarization direction in the orbit plane and perpendicular to it, respectively. When we are looking only for the radiation in-plane ($\theta = 0$) only the former is kept, thus the polarization direction stays on the orbit plane.

$$\vec{r}(t) = \left(\rho\sin\frac{\beta c}{\rho}t, \rho\left(1-\cos\frac{\beta c}{\rho}t\right), 0\right) \quad , \quad \xi = \frac{\rho\omega}{3c\gamma^3}(1+\gamma^2\theta^2)^{3/2} \tag{2.11}$$

$$\frac{d^3W}{d\Omega d\omega} = \frac{q^2}{16\pi^3\varepsilon_0 c}\frac{2\omega\rho}{3c\gamma^2}(1+\gamma^2\theta^2)\left[K_{2/3}^2(\xi)+\frac{\gamma^2\theta^2}{1+\gamma^2\theta^2}K_{1/3}^2(\xi)\right] \tag{2.12}$$

In our experiment we used the XDS beamline at LNLS-CNPEM [119], which provide hard x-rays ranging from 5 to 30 keV. We made use of a 6+2 circle diffractometer that allowed the sample to be rotated around all 3 axis, allowing a very complete investigation of the polarization dependence of the XAS spectra of our samples. (Fig. 2.6).
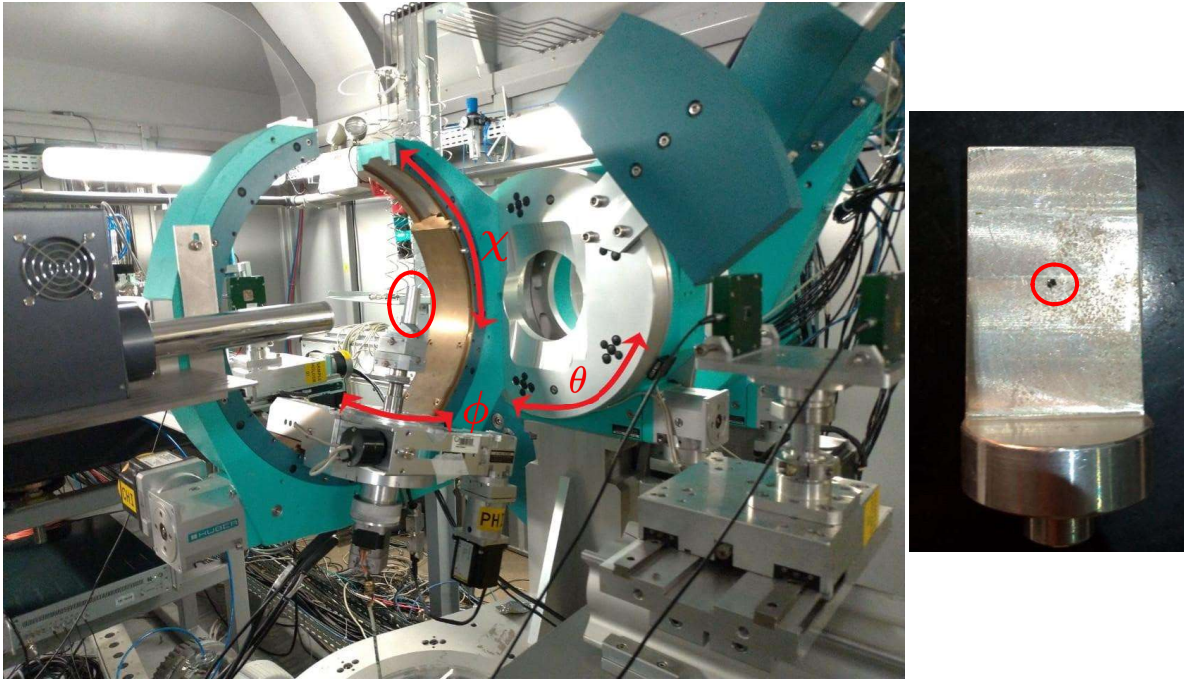
Fig. 2.6: (Left) The XDSs euler cradle, a 6+2 circle diffractometer, the angles used to probe the sample, and the support for the sample red circled. (Right) Support for the sample.

2.2 FEFF Calculations

FEFF 8.4 code was used to simulate the absorption effects and calculate the electronic structure. The FEFF code implements *ab initio* calculations of a self-consistent multiple scattering theory in real space (RSMS). The Green's function formalism is adopted and core-hole effects is taken into consideration. The code allows us to explore how different parameters contribute to the XAS spectra. Of special interest to the present work is the control of the exchange interaction parameters, the cluster size adopted to calculate the scattering potential, the possibility of making polarization dependent calculations and the projected local densities of states (LDOS). Several spectra types of X-ray based techniques can be calculated but in this work we dedicate our attention to the calculation of the XANES spectra. [120, 121].

The code can be broken into five main steps, namely (i) Dirac–Fock atomic calculation, (ii) potentials and densities, (iii) embedded atomic cross sections and phase shifts, (iv) calculation of the multiple-scattering Green's function, and (v) spectral calculations.

In all cases, the FEFF code adoots a local density approximation (LDA) to calculate the scattering potencial and electronic structure, and consider only one-electron transitions. Therefore, effects of electronic correlations are essentially not captures by this type of calculation. In this regard, agreement of the experimental spectra with FEFF calculations is usually interpreted as a sign of weak electronic correlations in the material.

Chapter 3

Results and Discussion

In the last chapter, we discussed in detail the experiments that we carried out at the LNLS XDS beamline. In this chapter, we present our main results and analyses. As a guide to the reader, we summarize some relevant point of the previous chapters:

- The Fermi surface properties of the FeScs is multiorbital and it is dominated by the Fe 3d orbitals. All relevant physics of the FeScs is due to states in the vicinity of the Fermi level.

- Our Fe K edge XANES experiments probe the Fe 3d orbitals in an indirect way. Indeed, it is only due to the Fe3dAs4p bybridization that we can probe the Fe 3d states. The As 4p orbitais are probed directly by the As K edge experiments.

- In our experiments, we choose to investigate the parent compound and samples that are, in principle, on either on the hole or electron doped sides of the phase diagram.

We split this chapter in two sections. First, we present our data and analyses based upon multiple scattering theory implemented by the FEFF code. Later, we present the results from quantum chemistry calculations, obtained in collaboration. Part of our conclusions and early assumptions are revised in view of the quantum chemistry calculations.

3.1 Data and FEFF XANES spectra analysis

In Fig. 3.1(c) and (d) are presented representative normalized ($\mu(E)$) Fe and As K edge spectra of BaFe$_2$As$_2$ along with their respective spectra derivatives. The Fe K-edge XANES spectrum presents five absorption features labeled by capital letters $A - E$. The features are positioned in the mid range between the maxima and minima of the spectrum derivative. Features $A - C$ are of electronic nature, while features D and E are predominantly due to scattering processes [57, 58, 59].

The A feature sits at about E_{F}, which is found to be $E_{\text{F}} \approx 7111.6$ eV. This feature is called the pre-edge and is understood to stem from a dipolar transition from the Fe $1s$ to Fe3dAs4p

hybrid bands. It comprises a series of energy levels located in a $1 - 2$ eV bandwidth about E_F and expresses the properties of the FeAs tetrahedral coordination complex. Feature C, at about ≈ 7118.6 eV, is the main atomic transition of the Fe K-edge and stem from Fe $1s \rightarrow 4p$ transitions. The Fe$4p$ orbitals are well above E_F and form metallic bands in the material.
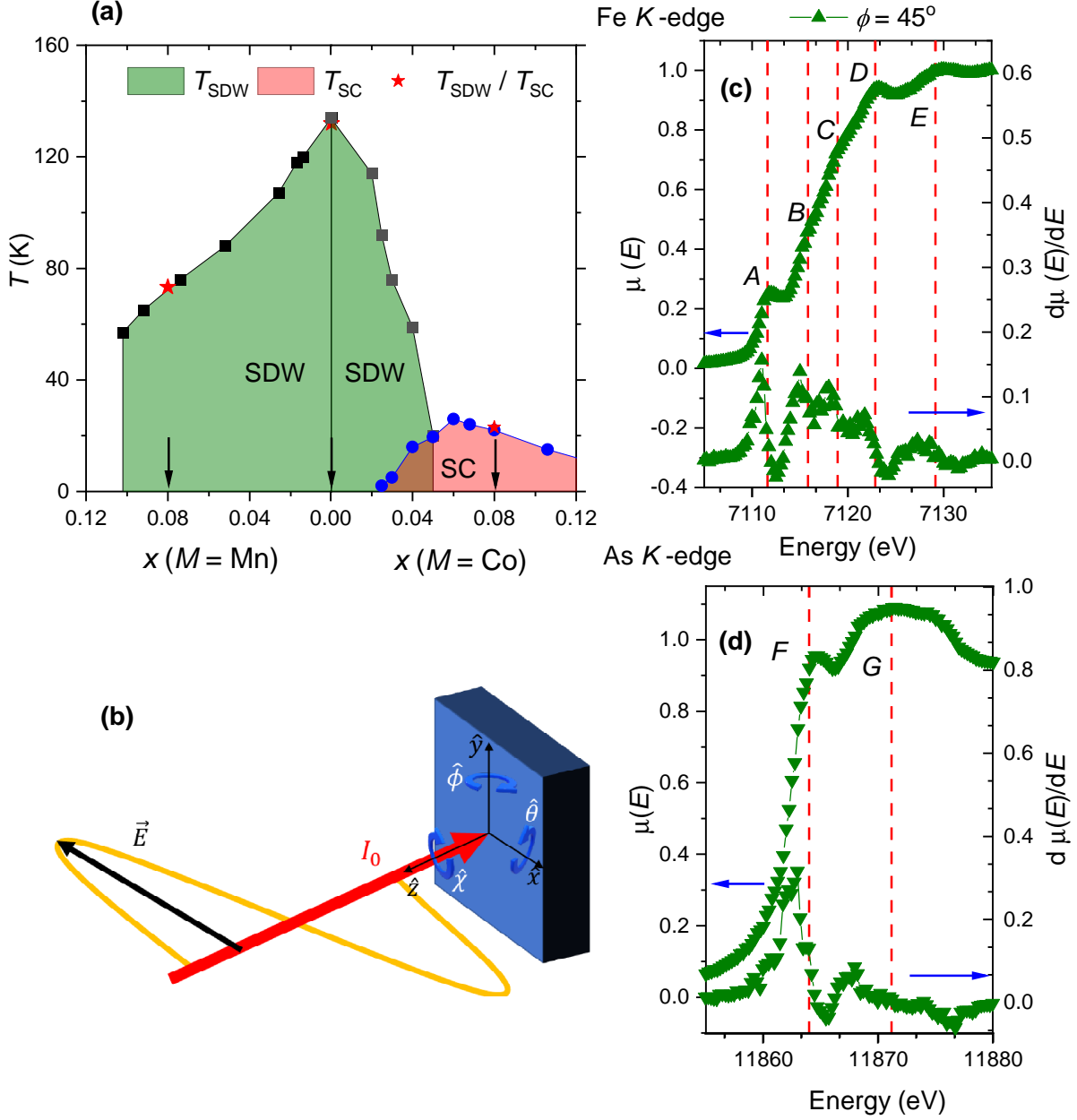
Fig. 3.1: (a) Composition (x) $vs.$ T phase diagram for the Ba(Fe$_{1-x}$Mn$_x$)$_2$As$_2$ and Ba(Fe$_{1-x}$Co$_x$)$_2$As$_2$ transition metal substituted iron arsenides. (b) Schematic representation of the experimental geometry, defining the rotation angles ϕ, θ and χ as rotations around the $\boldsymbol{x}$, $\boldsymbol{y}$ and $\boldsymbol{z}$ axis, respectively. (c) Representative Fe K-edge normalized XANES spectrum ($\mu(E)$, left axis) and its derivative ($d\mu(E)/dE$, right axis). Capital letters A-E mark the transitions and the dashed lines associate the features in the spectrum derivative to the spectrum. (d) The respective data for the As K-edge, with capital letters F-G labeling the absorption features.

The As K-edge XANES spectrum in Fig. 3.1(d) display two main features, which were called F and G. The former identify the main As $1s \to 4p$ atomic electronic transition which, due to the As coordination, also includes contributions from Fe $3d$ orbitals. The latter is mainly due to multiplet scattering processes and transitions to excited electronic states 6 eV above E_{F}. The F feature sits about $E_F \approx 11864.3$ eV.

In Fig. 3.2(a) − (c) it is presented the Fe K edgespectra of BaFe$_2$As$_2$ for all investigated rotations. In its local coordinate frame, rotating the sample is equivalent to change the incident beam polarization, which leads to new selection rules for the dipole transitions. A θ rotation is thus a control experiment, which does not change the beam polarization. Indeed, a direct inspection Fig. 3.2(a) reveal that θ rotations do not change the spectra. A χ rotation probes orbitals with planar components (as, for instance, the p-orbitals p_x and p_y) while ϕ rotations probe orbitals with z symmetry, as p_z orbitals.

The observed spectra intensity clearly increase under ϕ rotations (Fig.Fig. 3.2(b)) characterizing the spectra anisotropy. The inset in Fig.3.2(b) display the difference spectrum, obtained from making $\mu(E, \phi = 45°) - \mu(E, \phi = 0)$. As it is clear, the anisotropy is strong in the pre-edge (A feature) but persists in all regions of the electronic transitions, peaking again close to the main edge (C feature). The red arrow in the figure calls attention to the fact that the baseline of the spectra coincides in the region below the E_{F}, excluding a systematic shift of the background signal as a source of the effect.

The significant increase in the pre-edge intensity for a ϕ rotation, therefore, shows that the relative hybridization and occupation of the As $4p_{x,y,z}$ are not equivalent, suggesting that the As $4p_z$ orbitals hybridize to form states with a higher density of unoccupied states. The observed lack of in plane anisotropy for a χ rotation is expected since the p_x, p_y orbital degenaracy is not broken in tetragonal symmetry. In addition, the very observation of the XAS polarization dependence is to be noted, since in systems of itinerant electronic states the ligands are expected to be weak due to screening by conduction electrons. These results add to the importance of the local electronic properties of itinerant magnets [14].

In Figs.Fig. 3.2 (d) − (e), it is shown the As K-edge spectra data. Here, one can also observe that θ rotations do not change the spectra, which is also the case for χ rotations. Again, the spectra are clearly anisotropic for ϕ rotations, with the absorption edge becoming more intense. This result provides a direct assessment of the As $4p_z$ relative lower electronic filling and larger anisotropic orbital character. Calling attention to the red arrow in Fig. 3.2 (e), showing that the baseline of the spectra coincides in the region below the Fermi level. In the inset, it is shown the difference spectra which evidences the large anisotropy of both F and G features.
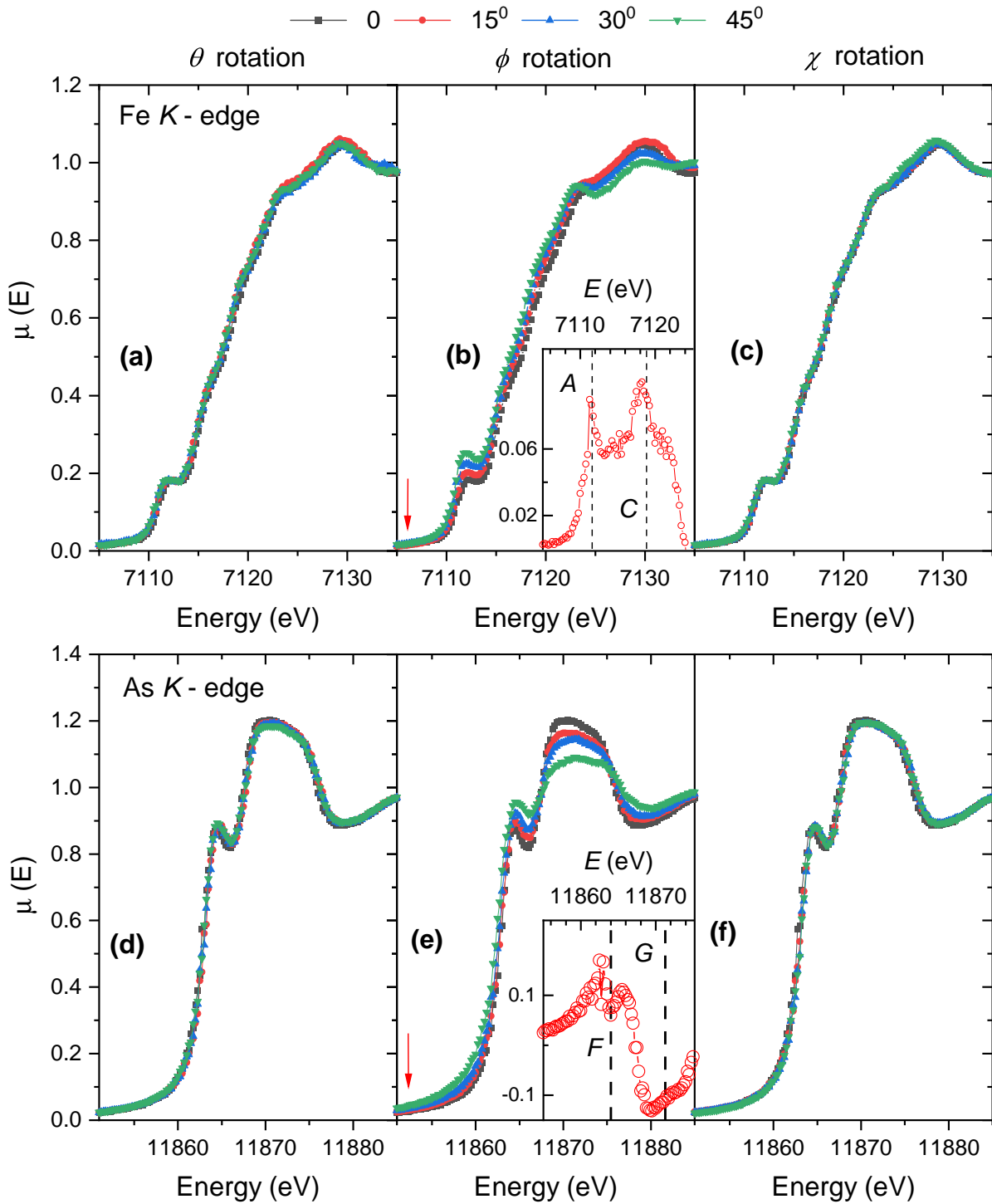
Fig. 3.2: $(a) - (e)$ Polarization dependence of the Fe K-edge and As K-edge XANES spectra of BaFe$_2$As$_2$. The open red circles in the insets of panels (b) and (e) show the difference spectrum $(\mu(E)_{\phi=45} - \mu(E)_{\phi=0})$ with the dashed lines marking some representative energy positions.

The next step is to investigate the composition dependence of the above effects. We start by inspecting the Fe K-edge of Mn and Co doped samples. Their XANES normalized spectra $(\mu(E))$ are presented in figures Fig. 3.3$(a) - (f)$. The Co doped sample is slightly overdoped with $T_{SC} \approx 22$ K while the Mn doped sample does not display SC (see Fig. Fig. 3.1(a)).

Their putative electronic effects, however, would be symmetric with respect to hole and electron doping making these samples ideal for our studies. Concerning θ and χ rotations, the results are similar to what was found in the parent compound, while the data for ϕ rotations suggest a weak composition dependency of this anisotropy.
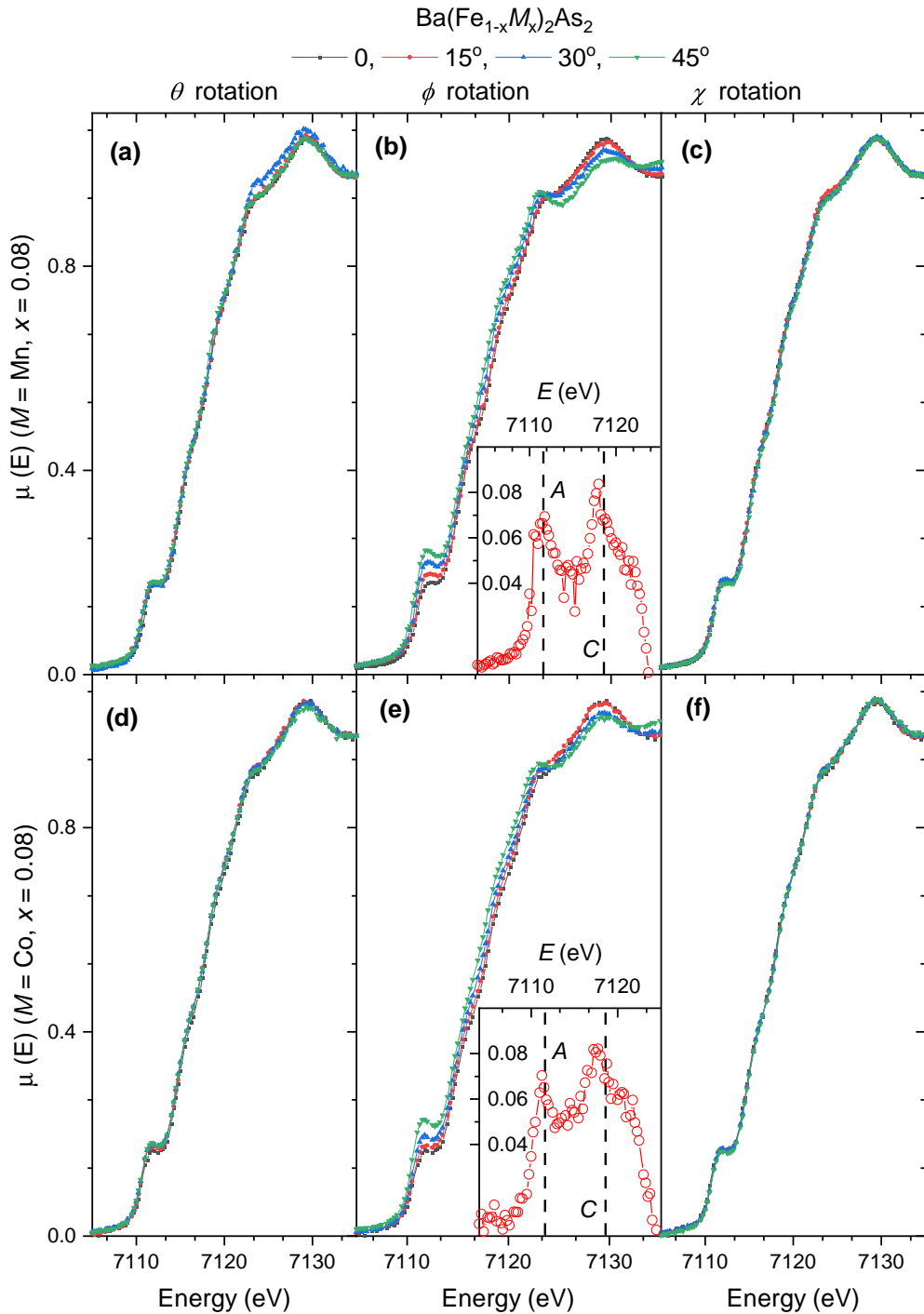
Fig. 3.3: Polarization dependence of the Fe K-edge XANES spectra of $(a) - (c)$ Ba(Fe$_{0.92}$Mn$_{0.08}$)$_2$As$_2$ and $(d) - (f)$ Ba(Fe$_{0.92}$Co$_{0.08}$)$_2$As$_2$ as a function of the polarization as indicated in figures. In all cases, the normalized intensities ($\mu(E)$) are presented. The open red circles in the insets of panels (b) and (e) show the difference spectrum ($\mu(E)_{\phi=45} - \mu(E)_{\phi=0}$) with the dashed lines marking some representative energy positions.

39

Indeed, in the case of the $Ba(Fe_{0.92}Mn_{0.08})_2As_2$ sample, the relative change of the pre-edge intensity is slightly more pronounced while the other edge features are comparable. The insets in figures Fig. 3.3(b) and (e) present the difference spectra for the Mn and Co substituted samples, respectively, and show this effect in more detail. Moreover, the C feature remains markedly anisotropic under ϕ rotations, showing that $Fe4p_z$ orbitals form bands with a higher unoccupied density of states than the $Fe4p_{x,y}$ orbitals. This particular result for the $BaFe_2As_2$ parent compound and doped materials is in contrast to the case of SmFeAsO [141]. In addition, as in previous XANES experiments of iron arsenides, the C feature is not much affected by Co-doping [57, 58, 89, 60] and is here shown to be unaffected by Mn doping as well.

Further investigation on the composition effect is shown in figure Fig. 3.4(a) − (c). To quantify the intensities anisotropy as a function of ϕ, the Fe K-edge spectra was fitted by a series of Lorentzian (the A_1 and A_2 peaks) and Gaussian (the B, C, D and E peaks) lineshapes plus a Fermi-Dirac function as in figure Fig. 3.4(a). The two peaks in the pre-edge region are clearly present in high-resolution experiments [60] and are suggested by the analysis of our spectra derivatives. Indeed, adopting two peaks is instrumental to extract a consistent fitting analysis. The resonance intensities I_{peak} are estimated from the peak areas, as in the shades of figure Fig. 3.4(a). In figures Fig. 3.4(b) − (c), respectively, were plotted the I_{A_1} and I_B normalized intensities as functions of ϕ for the compositions as indicated. Each data set is normalized as $I_{\text{peak}}(\phi)/I_{\text{peak}}(\phi = 0)$.

The A_1 peak of the Mn substituted sample is distinctly more anisotropic, but the composition effect is not present in the case of the B feature. Since the latter lies $\approx$ 3eV above E_F, it would be hardly affected by doping, as observed. A naive interpretation about the effect of Mn substitution is that Mn "doping" fills the $Fe3dAs4p$ hybrid bands with holes, increasing the amount of unoccupied states. At the present "doping" level, however, Mn impurities do not act as charge dopants to $BaFe_2As_2$ [152, 153] and we shall return to this discussion later.

In figure Fig. 3.4(d)−(f) we show polarization dependent FEFF calculations of the $BaFe_2As_2$ Fe K- edge. In figures Fig. 3.4(d) and (e), the calculated spectra and their derivatives are, respectively, compared to experimental data. The FEFF calculations capture the $B − E$ features position but the A feature, however, is not reproduced in our calculations. Indeed, FEFF calculations do not capture in full the properties of bound states [143, 144, 120]. In turn, the lack of the A feature on the FEFF calculated spectra further indicates the correlated nature of the $Fe3d$ states in our material. Even in the cases of features $B − E$, the spectra polarization dependence is not captured in full, which is investigated in greater detail in figure Fig. 3.4(f).

In figure Fig. 3.4(f), we take advantage of the real space nature of FEFF calculations and present results for distinct cluster sizes. As can be observed, the calculated spectra are almost isotropic for small clusters, with the effect developing for larger clusters. The presence of the electronic features B and C are reproduced even for the 4 atom cluster, which includes only the 4 As ligands, and becomes better defined for the larger clusters. Features D and E develop only for clusters including the first 4 Fe and 2 Ba neighbors respectively. The inset in this

figure shows the difference spectrum $(\mu(E)_{\phi=45} - \mu(E)_{\phi=0})$ from experiments and from FEFF calculations. The B and C features polarization dependencies are poorly reproduced for all clusters, while the data for the D and E features (and the XAS region at further higher energy) are well reproduced by the larger cluster calculations.
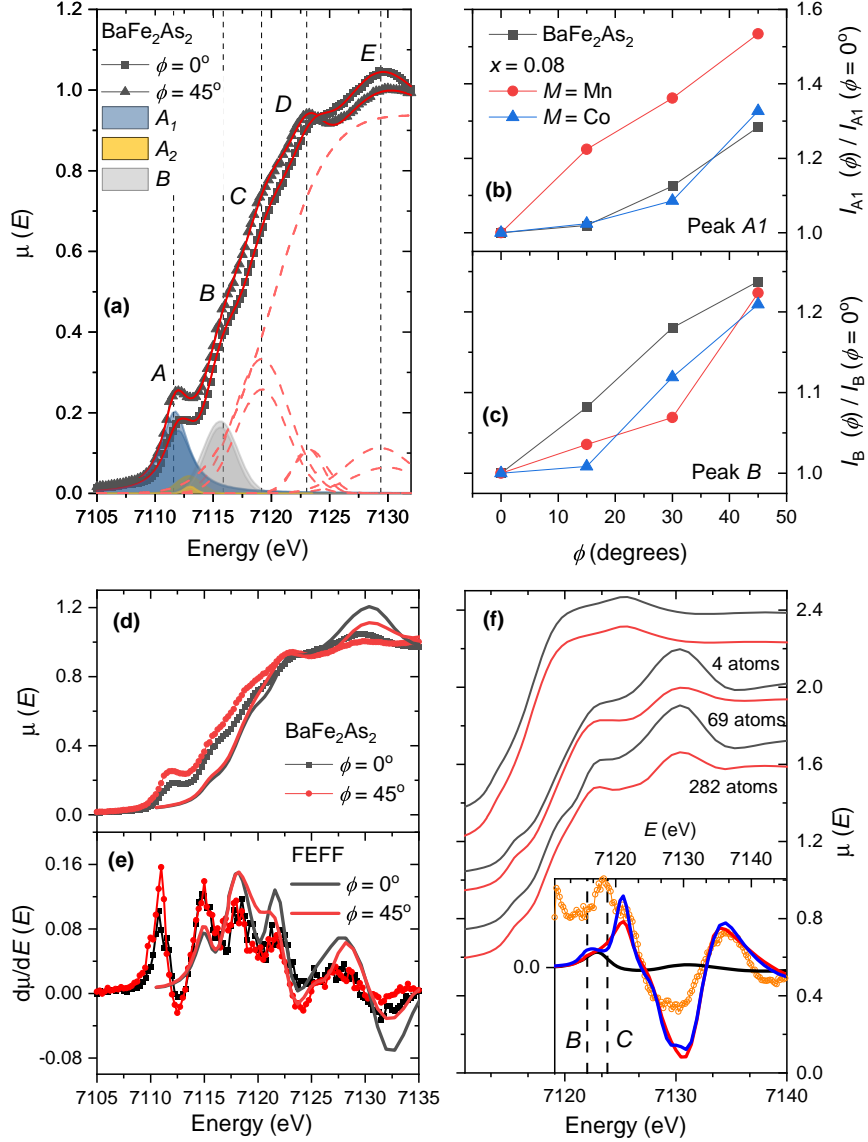
Fig. 3.4: (a) Fe K- edge XANES spectra of $BaFe_2As_2$ ($\phi = 0$ and $\phi = 45°$) and their respective phenomenological fittings. As shown, two peaks, termed A_1 and A_2 peaks are included to describe the pre-edge A feature. The shaded regions below the curves are the peak areas which are adopted to describe the resonance intensities. The obtained intensities are presented in (b) and (c) for, respectively, the A_1 pre-edge peak and the B edge peak as a function of ϕ and composition as indicated. In (d) and (e) we present polarization-dependent FEFF calculations of the Fe K-edge spectra and compare the results to experimental data. In panel (f), we show FEFF calculations for distinct cluster sizes as indicated. In the inset, we present the difference spectrum $(\mu(E)_{\phi=45} - \mu(E)_{\phi=0})$ from experiments (open orange circles) and the from FEFF calculations (black, red and blues lines are for 4, 69 and 282 atom clusters, respectively).

Now turning to the As K-edge experiments of other compositions. In Fig. 3.5$(a) - (f)$, the normalized intensities ($\mu(E)$) of the As K-edge XANES spectra of the doped samples are presented. Again, the measured spectra are isotropic under θ and χ rotations. In the case of ϕ rotations, however, both Ba(Fe$_{0.92}$Mn$_{0.08}$)$_2$As$_2$ and Ba(Fe$_{0.92}$Co$_{0.08}$)$_2$As$_2$ spectra are polarization-dependent but this time the composition is straightforwardly observed by direct inspection of Fig. 3.5(b) and (e). The inset of the same figures presents the respective difference spectrum ($\mu(E)_{\phi=45} - \mu(E)_{\phi=0}$). The insets are in the same scale, making it clear that the XANES anisotropy is larger for the Mn rich material. Moreover, it is also clear that edge anisotropy of the Co doped sample decreases when compared to the case of the parent compound, while it increases for the Mn containing sample. Since the As K-edge is a direct probe to the properties of the As $4p_{x,y,z}$ orbitals sitting at about E_{F}, the distinction between the localization and occupation of the As $4p_z$ orbitals should be more evident, as observed.

The anisotropy of the post edge feature at about 11870 eV, which is about 5 eV above the Fermi level, is also affected by composition, being less intense for the Co doped sample. This feature contains a series of contributions from As and Fe p states and Ba s states forming hybrid bands with d states from As and Ba atoms, as we shall see in the FEFF calculations for the As K-edge (see Fig. 3.6(e)). In all cases, it is more intense for the in plane polarization, indicating that it is dominated by unoccupied states of $4p_{x,y}$ symmetry. Since this feature is well above the Fermi level, the composition effect is most likely due to the direct effect of the impurity scattering potential and we conclude that Mn dopants act as stronger scattering centers when compared to Co dopants [154, 155].

To estimate the composition effect in the edge intensity anisotropy as a function of ϕ ($I(\phi)$), we adopt again the integrated areas of the edge features as the approximation to $I(\phi)$. This time, we make a direct integration of the experimental data, as exemplified in figure Fig. 3.6(a) in the case of the Mn doped sample. For each ϕ we obtain $I(\phi)$ and then we normalize the data as $I(\phi)/I(\phi = 0)$. Results for all samples are shown in figure Fig. 3.6(b). The error bars are estimated by small variations of the integration region. In comparison to the parent compound, the effect of Co doping is clear, while the effect of Mn doping is weak but significant.

In Ref. [89], Co doping is suggested to donate electrons to As derived orbitals. Here, we show that the electrons contributed by Co doping go preferentially to the unoccupied As$4p_z$ states, characterizing a distinct charge doping anisotropy by Co dopants. By adding electrons to orbitals along the c-axis, Co doping unbalances the electron and holes contributions to the transport along this direction, increasing the incoherent scattering in this direction. We thus support the interpretation given in Ref. [156] to the observed BaFe$_2$As$_2$ inter plane resistivity anisotropy and its increase with Co doping [157, 156]. Moreover, our results provide a real space picture of the evolving 3D character of the BaFe$_2$As$_2$ electronic structure as previously probed by angle resolved photoemission spectroscopy (ARPES) [158].
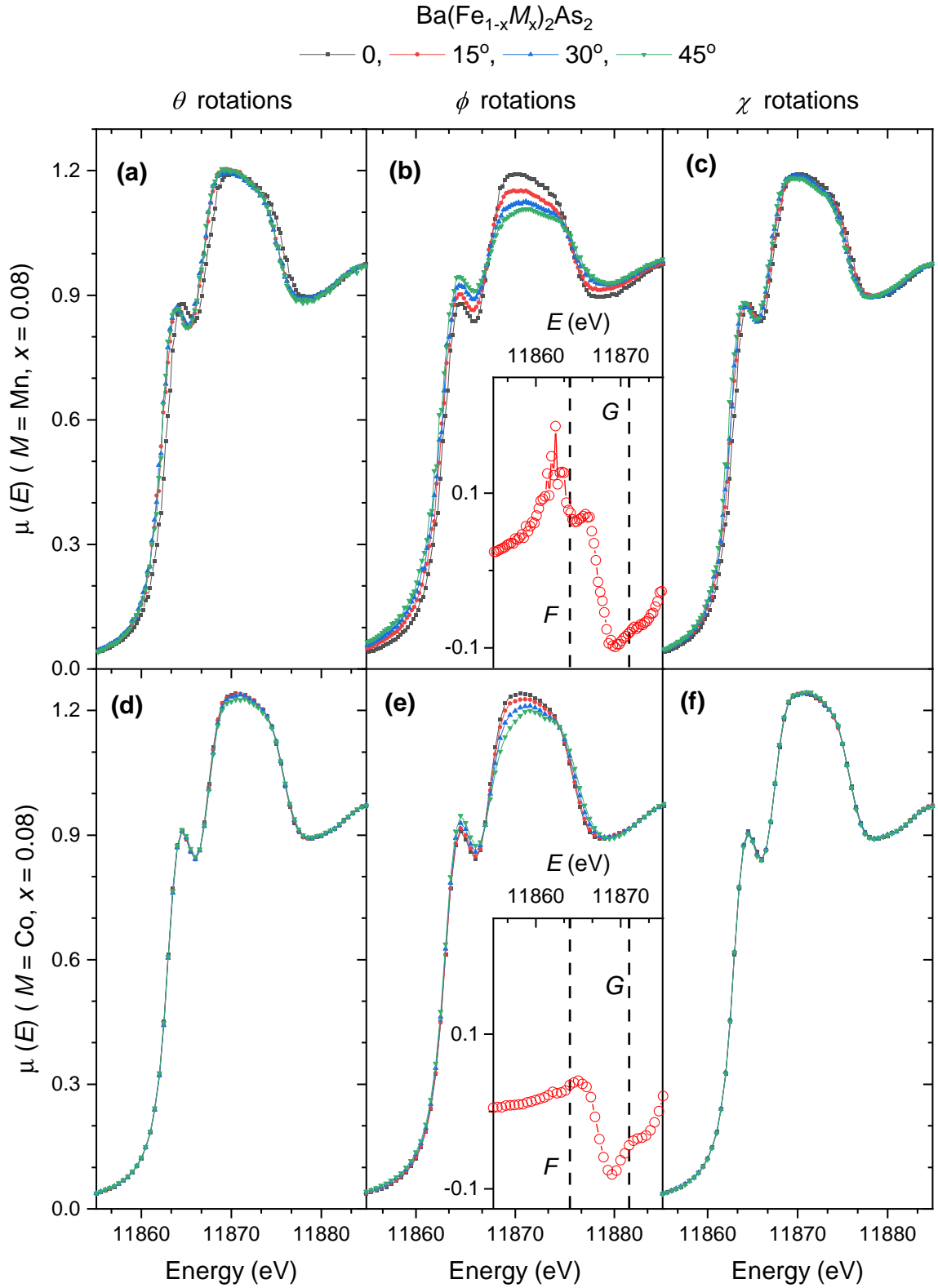
Fig. 3.5: Polarization dependence of the As K-edge XANES spectra of $(a) - (c)$ Ba(Fe$_{0.92}$Mn$_{0.08}$)$_2$As$_2$ and $(d) - (f)$ Ba(Fe$_{0.92}$Co$_{0.08}$)$_2$As$_2$ as a function of the polarization as indicated in figures. In all cases, the normalized intensities ($\mu(E)$) are presented. The open red circles in the insets of panels (b) and (e) show the difference spectrum ($\mu(E)_{\phi=45} - \mu(E)_{\phi=0}$) with the dashed lines marking some representative energy positions.

On the other hand, the mechanism for the anisotropy increase caused by Mn substitution cannot be ascribed to any change in the electronic filling, as above discussed. Supported by the above analysis of the As post edge feature, we interpret that, instead, Mn dopants are increasing the As$4p_z$ anisotropy because the orbitals are becoming more localized. This interpretation provides as well a mechanism for the localization of the Fe$3d$As$4p$ hybrid bands, with relevant consequences to Fe-derived electronic states. Indeed, resonant inelastic X-ray scattering (RIXS) experiments at the Fe L_3 edge could show that isoelectronic substitutions (P and Mn) can push BaFe$_2$As$_2$ to a correlated phase [147, 159].

To extract more information from our As K-edge experiments, we performed polarization-dependent FEFF calculations. We aim at describing two effects: the spectra anisotropy and the composition dependence of this effect. In figure Fig. 3.6(c) we compare the experimental and calculated As K-edges of BaFe$_2$As$_2$ for $\phi = 0$ and $\phi = 45°$. The overall spectral shape and anisotropy are well reproduced but there is a lack of detail in the effect of the anisotropy. In the calculations, the edge peaks nearly coincide while in the experiments the edge intensity of the $\phi = 45°$ spectra sits above the $\phi = 0$ spectra for all compositions. The absorption features relative positions are well reproduced by calculations, as can be observed in the spectra derivatives shown in figure Fig. 3.6(d).

To simulate the effects of chemical substitution, we performed FEFF calculations replacing one in ten Fe atoms with a dopant (either Mn or Co). This is equivalent to a $x = 0.1$ composition, which is close to our samples for which $x = 0.08$. Three dopant distributions were calculated and then averaged out. In the inset of figure Fig. 3.6(d), we compare the difference spectrum ($\mu(E)_{\phi=45} - \mu(E)_{\phi=0}$) obtained from the BaFe$_2As_2$ data (open red circles) and from FEFF calculations of the parent compound and substituted samples (thick lines). As can be observed, the edge polarization dependence is partially reproduced but only a small composition effect is observed in the FEFF calculations.

In figure Fig. 3.6(e), we show the element (site projected) and orbital projected local density of states (LDOS) obtained from FEFF calculations. At the top of the panel, the FEFF calculated As K-edge spectrum BaFe$_2$As$_2$ is reproduced for comparison. It shows that the main edge is dominated by As $4p$ states, as expected. Moreover, the high density of Fe $3d$ states about the edge position allows the formation of Fe$3d$As$4p$ hybrid bands making the As K-edge transition sensitive to this mixing. In the case of the post edge G feature, it is suggested that it is comprised by a series of contributions from As and Fe p states and Ba s states forming hybrid bands with d states from As and Ba atoms.

FEFF calculations give a fair description of the one-electron scattering in the cluster scattering potentials which is here calculated for a large self-consistent radius. In this context, the effects of electronic filling due to either Mn or Co impurities should be described by FEFF, but is here observed to be much weaker than what is observed in experiments. Therefore, our FEFF analysis further supports that the effects of Mn and Co substitutions do not fit in a simple rigid band shift scenario.
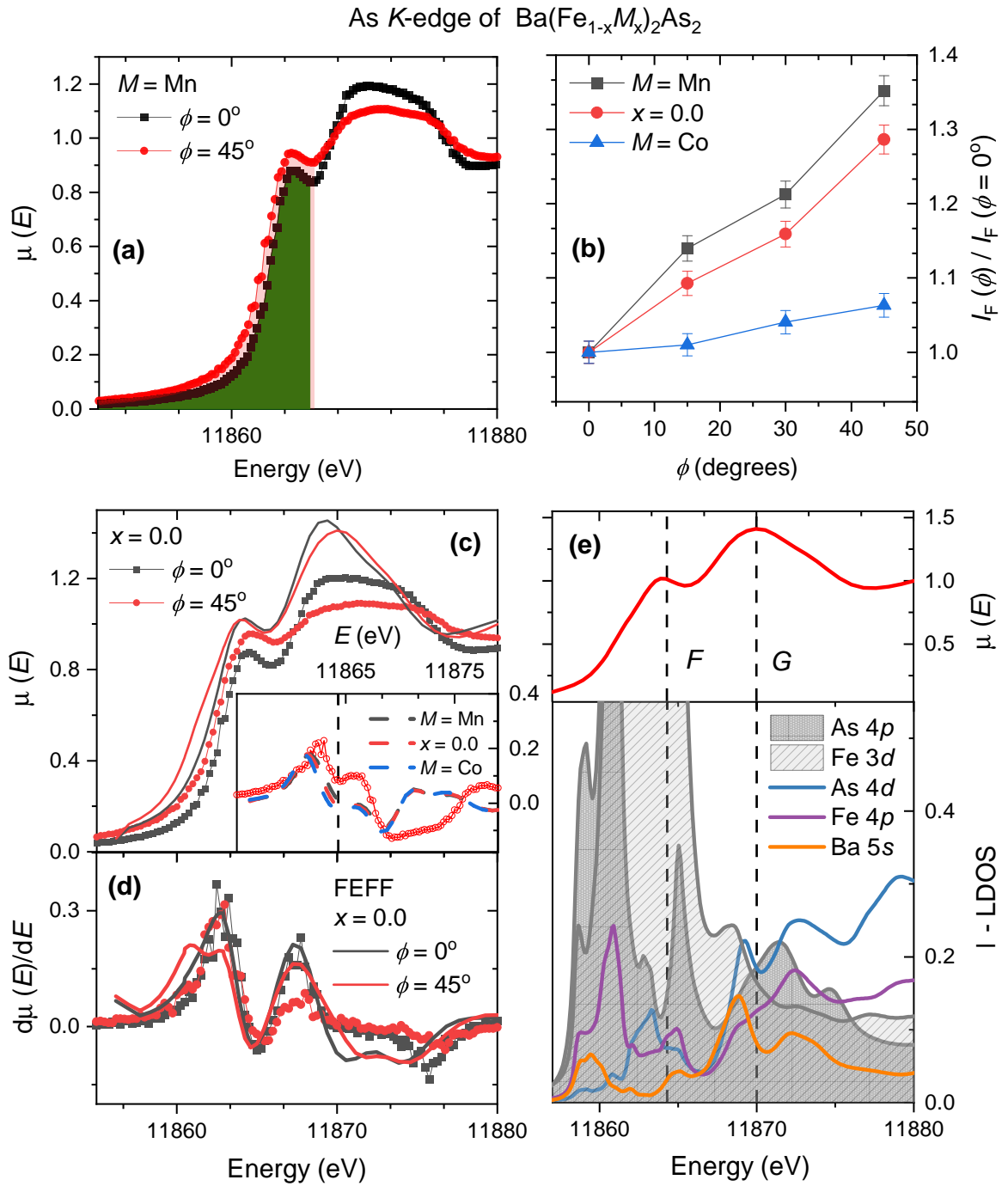
Fig. 3.6: (a) Normalized intensities ($\mu(E)$) of the As K-edge XANES spectra of Ba(Fe$_{0.92}$Mn$_{0.08}$)$_2$As$_2$ for $\phi = 0$ and $\phi = 45°$. In each case, the panel shows the spectrum region taken into consideration to perform the numerical integration that represents the F feature intensity ($I_F(\phi)$). (b) The polarization dependence of the F peak intensity as a function of ϕ, for all compositions. (c)-(d) Polarization-dependent FEFF calculations of the As K-edge of BaFe$_2$As$_2$ spectra compared to experimental data. The inset in panel (d) present the difference spectrum of the BaFe$_2$As$_2$ data (open red circles) compared to FEFF calculations of Ba(Fe$_{1-x}$M$_x$)$_2$As$_2$, with $M =$ Mn or Co and $x = 0.1$ (see main text). (e) FEFF calculated site and orbital projected LDOS of BaFe$_2$As$_2$. FEFF calculations of $\mu(E)$ are reproduced on the top of the LDOS calculations for comparison.

3.2 Quantum Chemistry Calculations

While our FEFF calculations for the Fe and As K-edges are able to support some aspects of our discussion of the experimental results, it is clear that many aspects of the physics of our system are not captured. This is nothing but an expression of the still unresolved character of the electronic states of the FePns materials, that lay in the border between strong and weak electronic correlations. We thus resort to quantum chemistry calculations of the electronic properties of a single $FeAs_4$ distorted tetrahedron, within a multiconfigurational calculation of the orbital states [145, 146, 150, 151]. These calculations were performed by an in group collaboration and its results were discussed by all group members collaborating in this project.

Being XANES a local probe to electronic structure, it is reasonable to assume that the electronic structure of a single $FeAs_4$ distorted tetrahedron can be connected to the pre-edge feature which, insofar as the Fe K-edge is concerned, is the main focus of our paper. Our results are presented in figure Fig. 3.7 and in table Tab. 3.1.

The multiconfigurational calculations results show that the first set of unoccupied states are indeed ligand field (or crystal field) levels formed by hybrid orbitals from Fe$3d$ and As$4p$ states. In our discussion, we name the $|a_1^*\rangle$, $|b_2^*\rangle$, $|e^*\rangle$ and $|b_1^*\rangle$ molecular orbitals by their Fe $3d$ main character, respectively, d_{z^2}, d_{xy}, d_{xz}/d_{yz} and $d_{x^2-y^2}$. The calculated ligand field splitting of only ≈ 0.3 eV is in qualitative agreement with previous calculations [160].

From table Tab. 3.1 and from the isosurface plot of the molecular orbital wavefunctions in figure Fig. 3.7, one can observe that all d_{xy}, d_{xz}/d_{yz} and $d_{x^2-y^2}$ hybridize with the As $4p_{x,y,z}$ orbitals. The d_{z^2} and d_{xy} orbitals appear in our calculations as nearly degenerate states and are indicated to be virtually double occupied. Electronic transitions are thus dominated by the d_{xz}/d_{yz} and $d_{x^2-y^2}$ hybrid orbitals.

	Iron orbitals (MO symmetry)	$3d_{z^2}$ (a_1^*)	$3d_{xy}$ (b_2^*)	$3d_{xz}, 3d_{yz}$ (e^*)	$3d_{x^2-y^2}$ (b_1^*)
	Ligand Field Relative energies / eV	0.000	0.002	0.260	0.308
2*Fe orbitals	$4p_z$			4.48	2.25
	$4p_y$ and $4p_x$	5.80		10.32	5.80
2*As Orbitals	$4p_z$	2.75		2.00	2.38
	$4p_y$ and $4p_x$	0.89	4.15	7.79	5.80

Tab. 3.1: Metal and ligand orbital composition of the $FeAs_4$ ligand field molecular orbitals. Numbers are given in percentage of normalized wavefunctions. The Final orbital composition analysis was performed adopting the Ros-Schuit partition method via the Multiwfn program [164].

All the d_{xz}/d_{yz} and $d_{x^2-y^2}$ display contributions with p_z orbital character and therefore contribute to the increase of the spectra intensity for ϕ rotations. It should be noted that even if the d_{xy} orbital were not double occupied, it would not contribute to this, since they present no mixing with p_z orbitals. The calculated hybridization pattern of the ligand field orbitals is

imposed by the specific properties of the FeAs$_4$ complex. Indeed, the D_{2d} symmetry would allow the mixing of p_z orbitals into the d_{xy} orbital, while it would prevent any p_z orbital mixing with $d_{x^2-y^2}$.
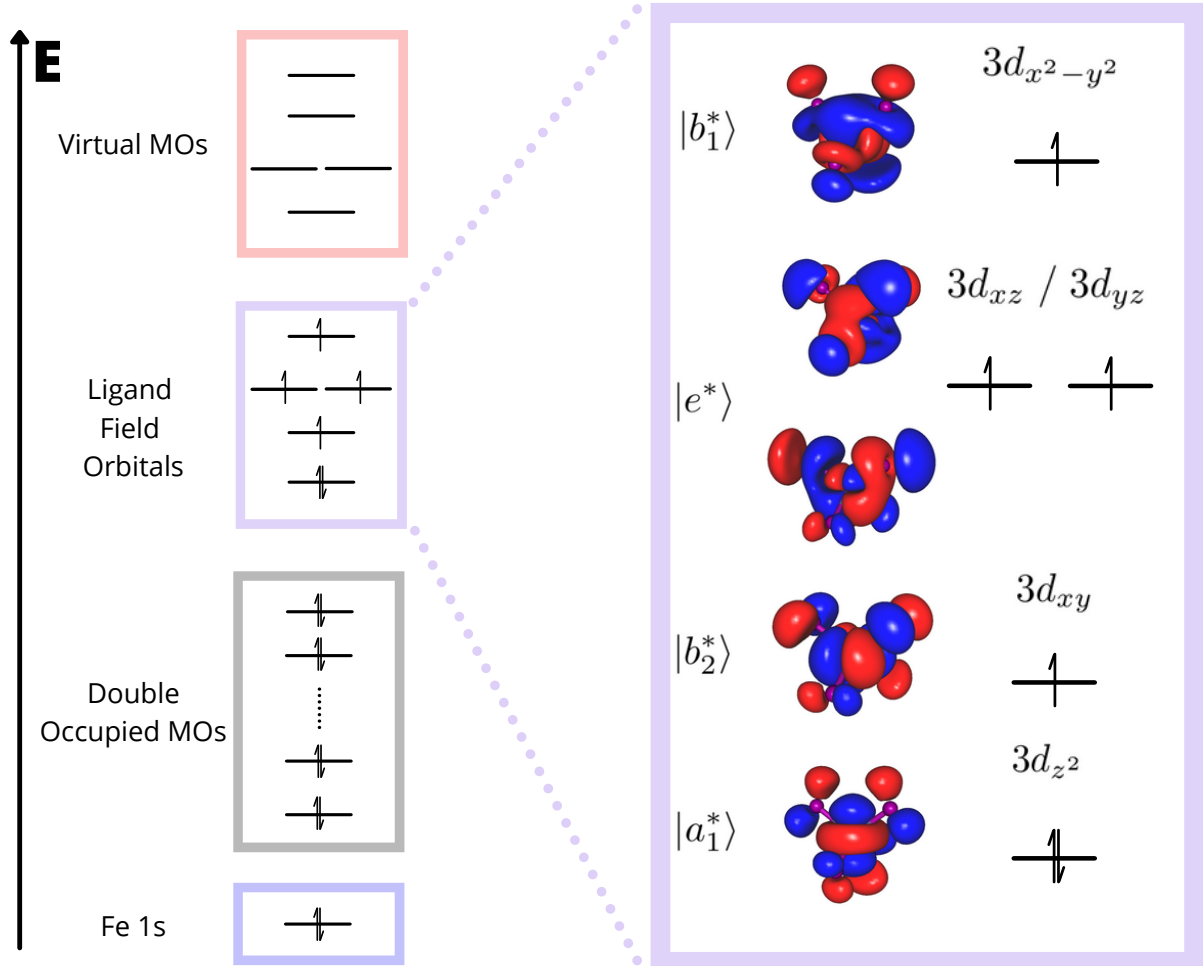
Fig. 3.7: Left panel: energetic ordering of fully occupied, ligand field and virtual orbitals as obtained from our calculations. Right panel: ligand field molecular orbitals and their ground state configuration based on CAS(6,5)/NEVPT-2/Def2-TZVPP approach [150]. Isosurfaces values are set to 0.006. Our results indicate a ligand field splitting of 0.308 eV. Ligand Orbitals are plotted via the Gabedit program [163].

The most prominent feature to be observed from the calculations, is the contribution from the Fe4p states to ligand field orbitals, forming Fe3d4p hybrid states. This local pd hybridization is acquired by the Fe3d states as a formal way of reducing their antibonding character, which is implied by the As^{-3} π-donation. This effect is a mechanism for the localization of the Fe3d states, as observed in other coordination complexes [161]. As a consequence, the pre-edge peak in the Fe K-edge can be attributed to Fe3d4p hybridization in Fe complexes [162] and our findings propose that we should reconsider the nature of the pre-edge transition of the Fe K-edge of the FePns materials. Indeed, so far in our discussion, as well as in previous works [86, 133, 139, 140, 141], the contribution of the Fe4p states to the pre-edge was overlooked. We shall argue that this local hybridization is key to understand the effects of Mn substitution.

First, we expect that via the Fe$3d$As$4p$ mixing, the Fe K-edge results should mirror that of the As K-edge, as observed. This expectation, however, does not take into account that the pre-edge intensity may be dominated by transitions to the Fe$3d4p$ states. This is likely the case of FeSe materials [142], for which the Se K-edge clearly indicates that the Se$4p_{x,y}$ planar orbitals dominate the density of unoccupied states, while the contrary is concluded from the Fe K-edge.

Mn substitution may weak the Fe$3d$As$4p$ mixing, making the Fe orbitals more localized through the mechanisms above explained. In turn, this would make the Fe$3d4p_z$ mixing stronger, increasing the observed polarization dependence. In the same direction, the As $4p$ will also become more localized, rendering the As K edge spectra more anisotropic. Both effects are observed in figures Fig. 3.4(b) and Fig. 3.6(b) and we propose that this is the mechanism related to Mn substitution in BaFe$_2$As$_2$: Mn impurities localize the Fe$3d$ states by changing the Fe$3d$As$4p$ mixing. In turn, it shows that hole doping is not the only active mechanism pushing BaFe$_2$As$_2$ to a more correlated Mott phase.

Chapter 4

Summary and Conclusions

This last chapter will be split into two parts: the first one containing the experimental overview and results, which mainly concerns the polarization dependence of the experimental XAS; and a second one, where we shown a quick roadmap of the FEFF results and its implications. In this roadmap we shall discuss how we eventually reached an understanding about the results from FEFF calculations.

4.1 Experimental Work

We have investigated the polarization dependence of the Fe and As K-edges XANES spectra of $BaFe_2As_2$ and chemically substituted Mn and Co materials of this parent compound. In the case of the Fe K-edge, we focused our analysis on the transitions allowed by Fe3dAs4p hybrid orbitals that spam the pre-edge structure of the Fe K-edge spectra. In the case of the As K-edge, we focused on the edge transitions, probing the As $4p_{x,y,z}$ orbitals.

The polarization dependence indicates that Co doping populates preferentially the hybrid bands with unoccupied states along the c axis (p_z orbitals), as concluded from the strong reduction of the As K-edge anisotropy. This is a distinct anisotropic charge doping effect, which may be connected to the transport properties and ARPES experiments of Co doped $BaFe_2As_2$ [156, 157, 158].

Mn substitution, while not changing the material electronic filling, increases the anisotropy of the probed electronic states. We attributed this finding to a delicate interplay between the local Fe3d4p and the metal-ligand Fe3dAs4p mixings, with Mn substitution favoring the Fe3d localization by hindering the Fe3dAs4p mixing.

In all cases, the XANES polarization dependence revealed a higher density of unoccupied state for orbitals with p_z character, with the results from the Fe K-edge mirroring those of the pnicitide K-edge. Our quantum chemistry calculations show this is not the only result that could be expected, since the local Fe3d4p hybridization also contributes to the pre-edge transitions and may dominate its polarization dependence. This is likely the case of FeSe materials [142]. One

can thus state a clear distinct behavior of the electronic states of iron arsenides and selenides, with the former presenting a stronger Fe$3d$As$4p$ hybridization, which favors the occupation of orbitals with planar geometry, while orbitals along the c-axis remain unoccupied. Our findings thus suggest that interplay between the local Fe$3d4p$ and the metal-ligand Fe$3d$As$4p$ mixings is common thread of the FePns electronic structure, unveiling the key role played by Fe $4p$ states.

4.2   FEFF Studies

Over the time we were trying to reproduce our XANES spectra through FEFF calculations, one of the investigations of how each parameter could affect it has lead us into a decisive question: which features on our simulations were we looking at?

The real part of the exchange correlation potential V_r was responsible for a constant shift on the Fermi level, thus being able to modify the displayed features. More concerning, the pre-edge features. After an extensive study on this parameter, we were able to identify two main scenarios, the first where we do reproduce a pre-edge for $V_r = 3.15$ (Fig. 4.1), presupposed correctly, and another where we don't for $V_r = -1.25$ (Fig. 4.2). Although it is known that FEFF can simulate pre-edges, they could be there for the wrong reason, as the code is limited to the (extended) continuum spectrum beyond the Fermi level, which means that the bound states are not generally included.

To settle down which way we were going, the polarization dependence was analyzed. In the case where the pre-edge is found, it was expected to see an increase in the intensity from $\phi = 0°$ to $\phi = 45°$, as seen in the experiment. However, that's not the case for any value of V_i between 0 and 1 (more values were tested and omitted for a better view), the potentials pure imaginary "optical" part, responsible for the an uniform decay, essentially the smoothness of the transition peaks. This is a decent evidence that the observed pre-edge on the simulations isn't driven by the right mechanisms, being an artifact. Another argument that could be used is the fact that the resonance positions below the Fermi level in the FEFF calculations with a pre-edge do not match with the experimental data.

This has lead us to believe that the correct path is indeed the one where a pre-edge isn't displayed. The fact the FEFF do not offer a fair description of the Fe K-edge data, turned out to be rather relevant to our idea to relate our experimental results to quantum chemistry calculations, as presented in the previous chapter and in our conclusions.
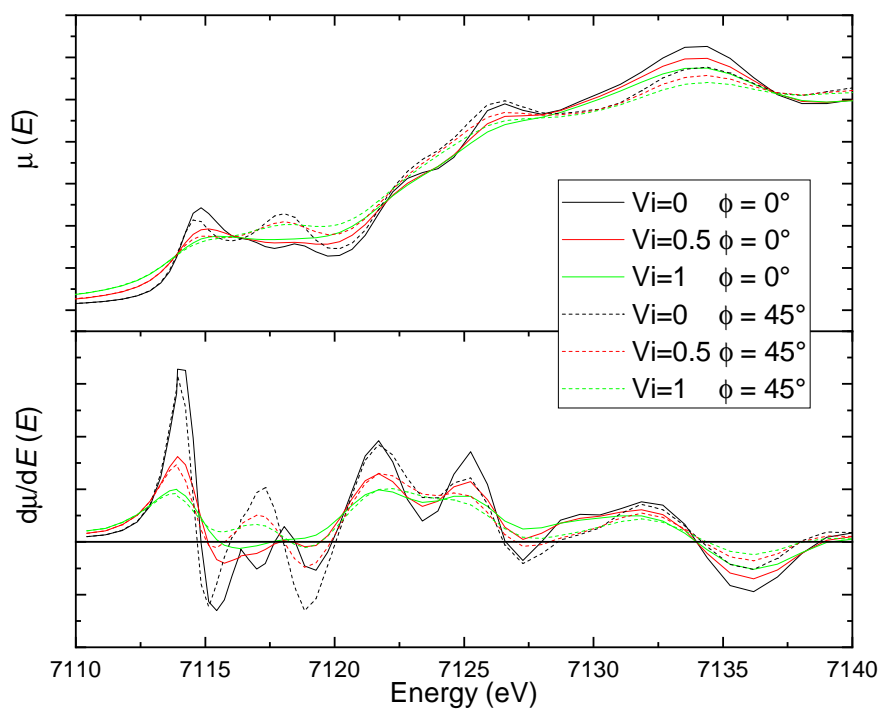
Fig. 4.1: For the pure sample at the Fe K-edge, FEFF calculations with different values of V_i of 0 (black), 0.5 (red) and 1 (green), for $V_r = 3.15$. Continuous lines for $\phi = 0°$ while dashed lines are for $\phi = 45°$.
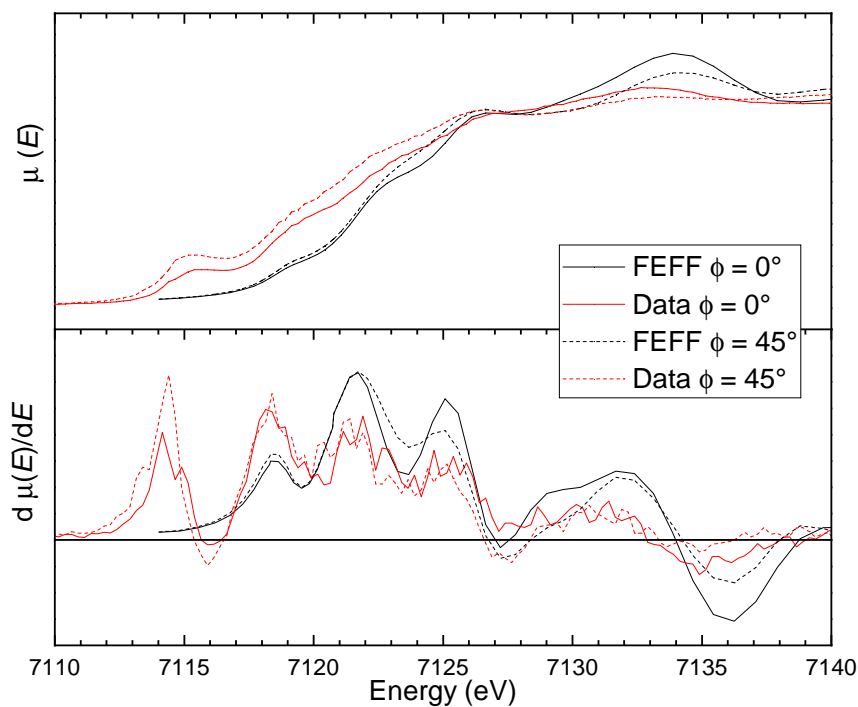
Fig. 4.2: For the pure sample at the Fe K-edge, FEFF calculations in black and experimental data in red, with continuous lines for $\phi = 0°$ while dashed lines are for $\phi = 45°$. A value of $V_r = -1.25$ was used.

Appendix A

Diamond Anvil Cell

A.1 Concept

It is possible to perform experiments under high-pressure in few ways, one of them had its initial concept first developed by Percy W. Bridgman in 1905 known as *Bridgman anvils*. The sample is compressed between two tungsten carbide (WC) anvils, which goal is to increase the pressure applied with the help of hydraulic press, reaching up to few GPa [122]. It was only in 1958 that the WC anvils were replaced by diamond anvils, giving birth to the *Diamond Anvil Cells* (DAC) [123], which with further improvements would allow pressures in the range of hundreds of GPa. Another integral part of the design of DACs that can be noticed Fig. A.1 is the *gasket*. This is a metal disk whose goal is to contain both the sample and a pressure medium, which in the end what allows one to perform experiment with hydrostatic pressure on the sample. This pressure medium depends on the desired pressure range for the experiments, with silicon oil and methanol-ethanol mixtures being among the most common ones. Within the gasket chamber it is also usual to insert a small piece of ruby, which helps on the temperature and pressure calibration via its fluorescence lines.

Fig. A.1: (Left) Bridgman anvil cell concept, where the sample is compressed by two WC anvils, increasing the pressure applyed by the hydraulic press. (Right) Diamond Anvil Cell concept, where the anvils are now made of diamonds. The gasket allows a filling around the sample, called the pressure medium, which helps creating a hydrostatic pressure, adapted from [124].
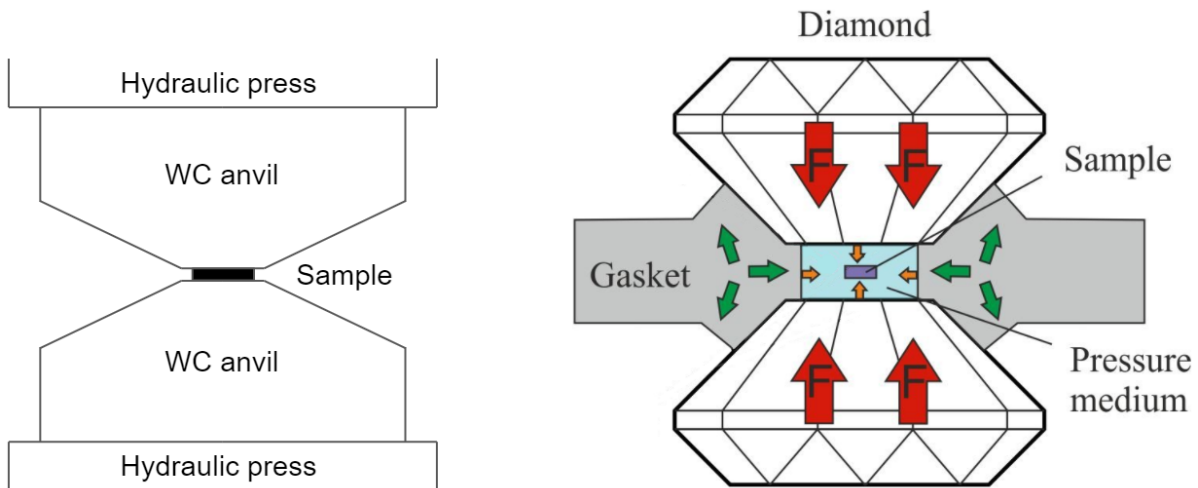
The use of DACs quickly spread mainly because of two reasons: i) the new high-pressure ranges and ii) because its anvils are made of diamond, which is transparent to a large range in the electromagnetic spectrum, therefore being a good device for experiments with x-rays, such as spectroscopy. With the rush on this new-found path, many designs were developed, but all of them can be understood as being focused on one of two different experimental geometries, the transmission\axial and the reflection\radial (Fig. A.2). Each one of them has it owns advantages and disadvantages. For example, the former has a lower mass, lower angle opening and it gives better results for thinner samples, and the latter has a higher mass, higher angle opening and allows thicker samples (Fig. A.3). All these parameters have to be taken into account when planning the experiment, as well as the material the DAC is made, which can influence in, for instance, magnetic properties measurements or in the temperature control. In addition, the DAC aperture angle is a critical parameter in x-ray scattering experiments, since it restricts the available region in the reciprocal space that can be probed.
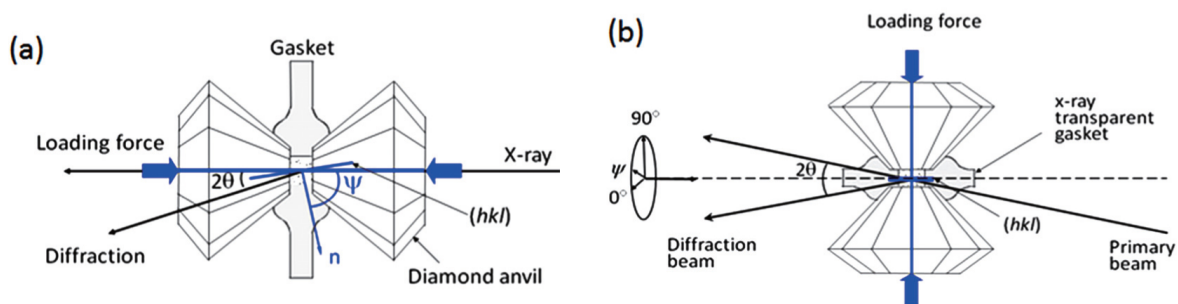

Fig. A.2: Two experimental setups for the DACs, (a) transmission (axial) where the beam goes through the diamonds and the sample, and (b) reflection (radial) geometry, where the beam goes through the gasket and the sample, adapted from [125].

DACs are essentially made of two pieces (Fig. A.3b) that fit perfectly together, each with a diamond of the same cullet size. Screws are added so that they don't rotate and misalign the diamonds, which would increase the odds of breaking them while also lowering the maximum pressure that can be applied with the device. The pressure on the sample can be remotely raised by a thin membrane on the top of the DAC, which is filled with liquid helium or nitrogen.

They can be used for a wide range of experiments, which includes but are not limited to, XAS, XRD, XANES, RXS, NRXMS and XMCD.
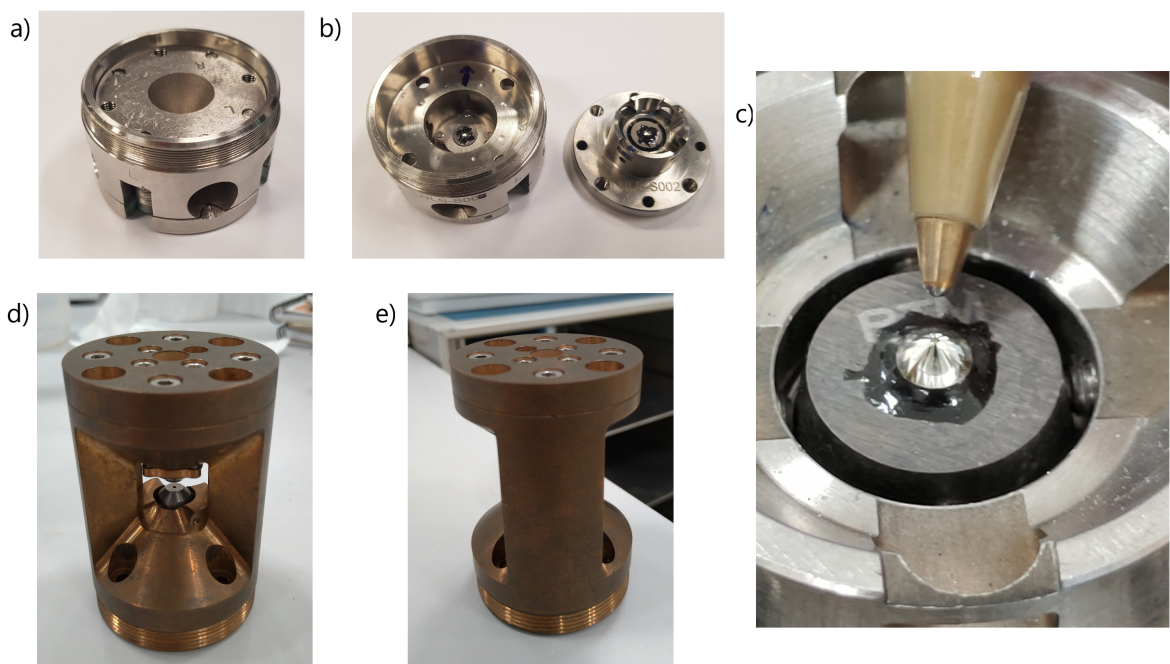
Fig. A.3: Examples of DACs models for both experimental setup geometries, used in CNPEM-LNLS. a) and b) shows a axial type closed and opened, respectively, with a width of 56mm and 32mm diameter. c) Close-up on the diamond, where the cullet (spot where the sample is compressed, with diameter ranging from 150μm to 900μm) can be seen and the ballpoint pen for size reference. d) and e) shows the panaromic cell optimized for the radial setup, made of beryllium-copper (BeCu).

As for the gasket, it also needs to perfectly fit both diamonds cullets, otherwise the experiment can be put in risk. For this a small disk made of stainless steel, beryllium-copper or rhenium is taken and indented with the diamonds (Fig. A.4a), and then taken into the electric discharge machine where the sample chamber will be created (Fig. A.4b-d). Rhenium gaskets are harder, being drilled using laser and with the proper safety protocols.
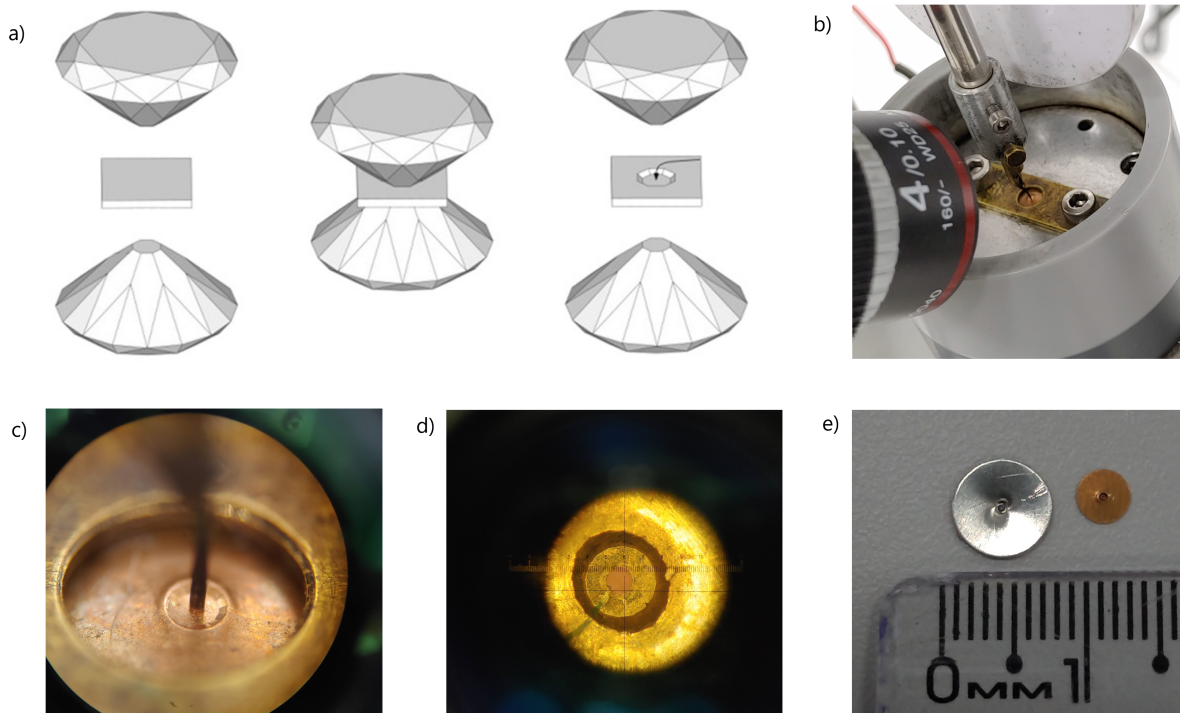
Fig. A.4: a) Schematic view of the indentation proccess, adapted from [126]. b-d) shows the sample chamber creation proccess via electric discharge, and e) is the finished gasket (stainless steel on the left and beryllium-copper on the right).

A.2   New Panoramic Cell Design

A DAC that is suitable for scattering experiments possesses a large angular aperture and is called a panoramic DAC. Although it is already possible to use the current panoramic cell displayed in Fig. A.3(d-e) in CNPEM, this existing device it is too heavy, handicapping the lowest temperature that can be reached in any cooling system. Moreover, it is also too large for the new cryostat recently manufactured for the new Sirius installations in CNPEM, hence the need of a new design that can take account of all these difficulties.

We have thus proposed a new design. The project was made using Autodesk® Inventor® CAD 2020 software, used for professional-grade 3D mechanical design, documentation, and product simulations, which includes mechanical stress analysis, that is one the most relevant parameters for the safe operation of the DAC.
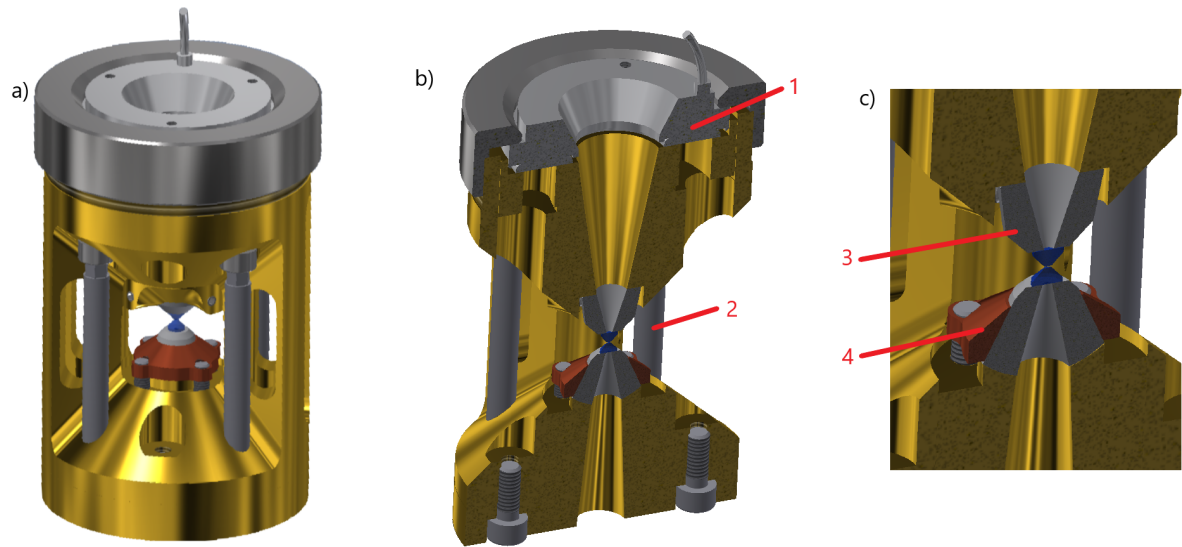
Fig. A.5: New panoramic cell design to be manufactured and tested. a) Full view, b) Half cutted and c) close-up on the center. Labeled in red we have 1-inflatable membrane for the pressure control, 2-auxiliary screws for the DACs assembly, being removed for the experiment, 3-WC seat and 4-WC rocker.

Due to the COVID-19 pandemic, the manufacturing and testing of the new panoramic cell was delayed. Still, the mechanical stress analysis was solid even using the default stainless steel and beryllium-copper alloy. The first prototype will be commissioned no latter than March/April of 2022 and will be available for experiments already in 2022.

Appendix B

Scientific Outputs

B.1 Papers

- Submitted: *"Orbital Localization and the Role of the Fe and As $4p$ Orbitals in BaFe$_2$As$_2$ Probed XANES"*.

  Authors: Alvaro G. de Figuereido, Marli R. Cantarino, Wagner R. da Silva Neto, Kevin R. Pakuszewski, Rogério Gossi, Denise S. Christovan, Jean C. Souza, Pascoal G. Pagliuso, Cris Adriano and Fernando A. Garcia.

- Submitted: *"ARPES experiments of Ba(Fe$_{1-x}$M$_x$)$_2$As$_2$ (M= Co or Cu): the role of transition metal substitution and Fermi surface properties at small x"*.

  Authors: Kevin R. Pakuszewski, Marli R. Cantarino, Alvaro G. de Figuereido, Lauro B. Braz, Mário M. Piva, Gabriel S. Freitas, Pascoal G. Pagliuso, Wendell S. Silva, Fernando A. Garcia and Cris Adriano.

B.2 Events

- Poster presentation at 28th RAU (Annual Users Meeting) of LNLS/CNPEM, *"The electronic structure of Ba(Fe$_{1-x}$TM$_x$)$_2$As$_2$(TM = Mn or Co) probed by XAS at the Fe and As K-edges: angular dependence"*.

Bibliography

[1] Y. Kamihara, T. Watanabe, M. Hirano and H. Hosono, *Iron-Based Layered Superconductor La[O1-xFx]FeAs (x = 0.05-0.12) with Tc = 26 K* (2008).

[2] J. G. Bednorz and K. A. Müller, *Possible high T_c superconductivity in the Ba-La-Cu-O system* (1986).

[3] M. Fowler, *Historical beginnings of theories of electricity and magnetism* (2012).

[4] R. M. White, *Quantum theory of magnetism magnetic properties of materials*, Springer (2006).

[5] P. W. Anderson, *New Approach to the Theory of Superexchange Interactions* (1959).

[6] J. B. Goodenough, *Magnetism And The Chemical Bond* (1963).

[7] B. T. Matthias and R. M. Bozorth, *Ferromagnetism of a Zirconium-Zinc Compound* (1958).

[8] B. T. Matthias, A. M. Clogston, H. J. Williams, E. Corenzwit, and R. C. Sherwood, *Ferromagnetism in Solid Solutions of Scandium and Indium* (1961).

[9] E. Svanidze, J. K. Wang, T. Besara, L. Liu, Q. Huang, T. Siegrist, B. Frandsen, J. W. Lynn, A. H. Nevidomskyy, M. B. Gamża, M. C. Aronson, Y. J. Uemura, and E. Morosan, *An itinerant antiferromagnetic metal without magnetic constituents* (2015).

[10] J. Kübler, *Theory of Itinerant Electron Magnetism*, Oxford University Press, Oxford (2009).

[11] P. Fazekas, *Lecture Notes on Electron Correlation and Magnetism* (1999).

[12] S. H. Simon, *The Oxford Solid State Basics* (2013).

[13] A. Lichtenstein, *Magnetism: From Stoner to Hubbard* (2013).

[14] B. Mounssef, M. R. Cantarino, E. M. Bittar, T. M. Germano, A. Leithe-Jasper, and F. A. Garcia, *Hard x-ray spectroscopy of the itinerant magnets RFe4sb12 (R=Na, K, Ca, Sr, Ba)* (2019).

[15] J. E. Hirsch, *Two-dimensional Hubbard model: Numerical simulation study* (1985).

[16] D. R. Penn, *Stability theory of the magnetic phases for a simple model of the transition metals* (1966).

[17] S. Brown and G. Grüner, *Charge and Spin Density Waves : Electrons in some metals arrange into crystalline patterns that move in concert, respond peculiarly to applied voltages and show self-organization* (1994).

[18] P. Monceau, *Electronic crystals: an experimental overview* (2012).

[19] J. Riera and D. Poilblanc, *Coexistence of charge-density waves, bond-order waves, and spin-density waves in quasi-one-dimensional charge-transfer salts* (2000).

[20] O. Madelung, *Introduction to Solid-State Theory* (1978).

[21] D. van Delft and P. Kes, *The discovery of superconductivity* (2010).

[22] W. Meissner and R. Ochsenfeld , *Ein neuer Effekt bei Eintritt der Supraleitfähigkeit* (1933).

[23] A. Orthacker, *Superconductivity*.

[24] I. Santoso, *k-space Microscopy of Bi2Sr2CaCu2O8+δ :Fermiology and Many-body Effects* (2015).

[25] N. Moloo, *Why High-Temperature Superconductivity Cannot Be Explained Without Quantum* (2016).

[26] M. S. Suzuki, *Superconductivity* (2019).

[27] J. Bardeen, L. N. Cooper, and J. R. Schrieffer, *Microscopic Theory of Superconductivity* (1957).

[28] P. J. Ray, *Structural investigation of La(2-x)Sr(x)CuO(4+y) - Following staging as a function of temperature* (2015).

[29] A. P. Drozdov, M. I. Eremets, I. A. Troyan, V. Ksenofontov and S. I. Shylin, *Conventional superconductivity at 203 kelvin at high pressures in the sulfur hydride system* (2015).

[30] Z. Z. Sheng and A. M. Hermann, *Bulk superconductivity at 120 K in the Tl–Ca/Ba–Cu–O system* (1988).

[31] A. Schilling, M. Cantoni, J. D. Guo and H. R. Ott, *Superconductivity above 130 K in the Hg–Ba–Ca–Cu–O system* (1993).

[32] G. R. Stewart, *Unconventional Superconductivity* (2017).

[33] P. J. Hirschfeld, M. M. Korshunov and I. I. Mazin, *Gap symmetry and structure of Fe-based superconductors* (2011).

[34] A. Chubukov, P. J. Hirschfeld, *Iron-based superconductors, seven years later* (2015).

[35] F. Steglich, J. Aarts, C. D. Bredl, W. Lieke, D. Meschede, W. Franz, and H. Schäfer, *Superconductivity in the Presence of Strong Pauli Paramagnetism: CeCu2Si2* (1979).

[36] C. Petrovic, P. G. Pagliuso, M. F. Hundley, R. Movshovich, J. L. Sarrao, J. D. Thompson, Z. Fisk and P. Monthoux, *Heavy-fermion superconductivity in CeCoIn5 at 2.3 K* (2001).

[37] E. Bauer, G. Hilscher, H. Michor, Ch. Paul, E. W. Scheidt, A. Gribanov, Yu. Seropegin, H. Noël, M. Sigrist, and P. Rogl, *Heavy Fermion Superconductivity and Magnetic Order in Noncentrosymmetric CePt3Si* (2004).

[38] R. C. Haddon, A. F. Hebard, M. J. Rosseinsky, D. W. Murphy, S. J. Duclos, K. B. Lyons, B. Miller, J. M. Rosamilia, R. M. Fleming, A. R. Kortan, S. H. Glarum, A. V. Makhija, A. J. Muller, R. H. Eick, S. M. Zahurak, R. Tycko, G. Dabbagh and F. A. Thiel, *Conducting films of C60 and C70 by alkali-metal doping* (1991).

[39] M. J. Rosseinsky, A. P. Ramirez, S. H. Glarum, D. W. Murphy, R. C. Haddon, A. F. Hebard, T. T. M. Palstra, A. R. Kortan, S. M. Zahurak, and A. V. Makhija, *Superconductivity at 28 K in RbxC60* (1991).

[40] A. F. Hebard, M. J. Rosseinsky, R. C. Haddon, D. W. Murphy, S. H. Glarum, T. T. M. Palstra, A. P. Ramirez and A. R. Kortan, *Superconductivity at 18 K in potassium-doped C60* (1991).

[41] Y. Kamihara, H. Hiramatsu, M. Hirano, R. Kawamura, H. Yanagi, T. Kamiya, and H. Hosono, *Iron-Based Layered Superconductor: LaOFeP* (2006).

[42] Y. Kamihara, T. Watanabe, M. Hirano, and H. Hosono, *Iron-Based Layered Superconductor La[O1-xFx]FeAs (x = 0.05-0.12) with Tc = 26 K* (2008).

[43] X. H. Chen, T. Wu, G. Wu, R. H. Liu, H. Chen and D. F. Fang, *Superconductivity at 43K in SmFeAsO[1-x]Fx* (2008).

[44] T. C. Ozawa and S. M. Kauzlarich, *Chemistry of layered d-metal pnictide oxides and their potential as candidates for new superconductors* (2008).

[45] H. Aoki and H. Hosono, *A superconducting surprise comes of age* (2015).

[46] K. Ishida, Y. Nakai and H. Hosono, *To What Extent Iron-Pnictide New Superconductors Have Been Clarified: A Progress Report* (2009).

[47] Z. Ren, G. Che, X. Dong, J. Yang, W. Lu, W. Yi, X. Shen, Z. Li, L. Sun, F. Zhou, *Superconductivity and phase diagram in iron-based arsenic-oxides ReFeAsO1-δ (Re = rare-earth metal) without fluorine doping* (2008).

[48] X. C. Wang, Q. Q. Liu, Y. X. Lv, W. B. Gao, L. X. Yang, R.C. Yu, F. Y. Li and C.Q.Jin, *The superconductivity at 18 K in LiFeAs system* (2008).

[49] C. W. Chuabc, F. Chena, M. Goocha, A. M. Guloyd, B. Lorenza, B. Lvd, K. Sasmala, Z. J. Tangd, J. H. Tappd and Y. Y. Xuea, *The synthesis and characterization of LiFeAs and NaFeAs* (2009).

[50] Z. Deng, X. C. Wang, Q. Q. Liu, S. J. Zhang, Y. X. Lv, J. L. Zhu, R. C. Yu and C. Q. Jin, *A new "111" type iron pnictide superconductor LiFeP* (2009).

[51] M. Rotter, M. Tegel and D. Johrendt, *Superconductivity at 38 K in the Iron Arsenide (Ba1-xKx)Fe2As2* (2008).

[52] K. Sasmal, B. Lv, B. Lorenz, A. M. Guloy, F. Chen, Y. Xue and C. Chu, *Superconducting Fe-Based Compounds (A1-xSrx)Fe2As2 with A = K and Cs with Transition Temperatures up to 37 K* (2008).

[53] P. M. Shirage, K. Miyazawa, H. Kito, H. Eisaki and A. Iyo, *Superconductivity at 26 K in (Ca1-xNax)Fe2As2* (2008).

[54] H. E. Toma, *Química de Coordenação, Organometálica e Catálise* (2016).

[55] *Non-octahedral Complexes* (2021).

[56] K. Momma and F. Izumi, *VESTA: a three-dimensional visualization system for electronic and structural analysis* (2008).

[57] E. M. Bittar, C. Adriano, T. M. Garitezi, P. F. S. Rosa, L. Mendonça-Ferreira, F. Garcia, G. de M. Azevedo, P. G. Pagliuso, and E. Granado, *Co-Substitution Effects on the Fe Valence in the BaFe2As2 Superconducting Compound: A Study of Hard X-Ray Absorption Spectroscopy* (2011).

[58] V. Baledent, F. Rullier-Albenque, D. Colson, G. Monaco and J.-P. Rueff, *Stability of the Fe electronic structure through temperature-, doping-, and pressure-induced transitions in the BaFe2As2 superconductors* (2012).

[59] M. Merz, F. Eilers, Th. Wolf, P. Nagel, H. v. Lohneysen and S. Schuppler, *Electronic structure of single-crystalline $Sr(Fe_{1-x}Co_x)_2As_2$ probed by x-ray absorption spectroscopy: Evidence for effectively isovalent substitution of Fe^{2+} by Co^{2+}* (2012).

[60] H. Yamaoka, Y. Yamamoto, J. Lin, J. J. Wu, X. Wang, C. Jin, M. Yoshida, S. Onari, S. Ishida, Y. Tsuchiya, N. Takeshita, N. Hiraoka, H. Ishii, K. Tsuei, P. Chow, Y. Xiao and J. Mizuki, *Electronic structures and spin states of $BaFe_2As_2$ and $SrFe_2As_2$ probed by x-ray emission spectroscopy at Fe and As K-absorption edges* (2017).

[61] H. Hosono, A. Yamamoto, H. Hiramatsua and Y. Ma, *Recent advances in iron-based superconductors toward applications* (2018).

[62] J. P. Sun, K. Matsuura, G. Z. Ye, Y. Mizukami, M. Shimozawa, K. Matsubayashi, M. Yamashita, T. Watashige, S. Kasahara, Y. Matsuda, J. -Q. Yan, B. C. Sales, Y. Uwatoko, J. -G. Cheng and T. Shibauchi, *Dome-shaped magnetic order competing with high-temperature superconductivity at high pressures in FeSe* (2016).

[63] Z. Wang, Y. Cai, H. Yang, H. Tian, Z. Wang, C. Ma, Z. Chen and J. Li, *Microstructure and structural phase transitions in iron-based superconductors* (2013).

[64] J. Dai, Q. Si, J. Zhu, E. Abrahams, *Iron pnictides as a new setting for quantum criticality* (2009).

[65] S. A. J. Kimber, A. Kreyssig, Y. Zhang, H. O. Jeschke, R. Valentí, F. Yokaichiya, E. Colombier, J. Yan, T. C. Hansen, T. Chatterji, R. J. McQueeney, P. C. Canfield, A. I. Goldman and D. N. Argyriou, *Similarities between structural distortions under pressure and chemical doping in superconducting BaFe2As2* (2009).

[66] M. D. Johannes, I. I. Mazin, and D. S. Parker, *Effect of doping and pressure on magnetism and lattice structure of iron-based superconductors* (2010).

[67] E. Granado, L. Mendonça-Ferreira, F. Garcia, G. de M. Azevedo, G. Fabbris, E. M. Bittar, C. Adriano, T. M. Garitezi, P. F. S. Rosa, L. F. Bufaiçal, M. A. Avila, H. Terashita and P. G. Pagliuso, *Pressure and chemical substitution effects in the local atomic structure of BaFe2As2* (2011).

[68] Y. Mizuguchi, Y. Hara, K. Deguchi, S. Tsuda, T. Yamaguchi, K. Takeda, H.Kotegawa, H. Tou and Y. Takano, *Anion height dependence of Tc for the Fe-based superconductor* (2010).

[69] S. Fujitsu, S. Matsuishi and H. Hosono, *Iron based superconductors processing and properties* (2012).

[70] C. H. Lee, A. Iyo, H. Eisaki, H. Kito, M. T. Fernandez-Diaz, T. Ito, K. Kihou, H. Matsuhata, M. Braden, K. Yamada, *Effect of Structural Parameters on Superconductivity in Fluorine-Free LnFeAsO1-y (Ln=La,Nd)* (2008).

[71] F. R.-Albenque, D. Colson, A. Forget and H. Alloul, *Hall Effect and Resistivity Study of the Magnetic Transition, Carrier Content, and Fermi-Liquid Behavior in Ba(Fe$_{1-x}$Co$_x$)$_2$As$_2$* (2009).

[72] W.L. Yang, A.P. Sorini, C-C. Chen, B. Moritz, W.-S. Lee, F. Vernay, P. O.-Velasco, J.D. Denlinger, B. Delley, J.-H. Chu, J.G. Analytis, I.R. Fisher, Z.A. Ren, J. Yang, W. Lu, Z. X. Zhao, J. van den Brink, Z. Hussain, Z.-X. Shen, and T.P. Devereaux, *Evidence for weak electronic correlations in iron pnictides* (2009).

[73] M.M. Qazilbash, J.J. Hamlin, R.E. Baumbach, L. Zhang, D.J. Singh, M.B. Maple and D.N. Basov, *Electronic correlations in the iron pnictides* (2009).

[74] H. Hosono, K. Kuroki, *Iron-Based Superconductors: current status of materials and pairing mechanism* (2015).

[75] A. Chubukov, *Pairing Mechanism in Fe-Based Superconductors* (2012).

[76] L. de' Medici, G. Giovannetti and M. Capone, *Selective Mott Physics as a Key to Iron Superconductors* (2014).

[77] Z. P. Yin, K. Haule and G. Kotliar, *Magnetism and charge dynamics in iron pnictides* (2011).

[78] Z. P. Yin, K. Haule and G. Kotliar, *Kinetic frustration and the nature of the magnetic and paramagnetic states in iron pnictides and iron chalcogenides* (2011).

[79] R. Yu, J.-X. Zhu and Q. Si, *Orbital-dependent effects of electron correlations in microscopic models for iron-based superconductors* (2013).

[80] M. Yi, D.H. Lu, R. Yu, S.C. Riggs, J.-H. Chu, B. Lv, Z. K. Liu, M. Lu, Y.-T. Cui, M. Hashimoto, S.-K. Mo, Z. Hussain, C.W. Chu, I.R. Fisher, Q. Si and Z.-X. Shen, *Observation of universal strong orbital-dependent correlation effects in iron chalcogenides* (2013).

[81] M. Yi, Z-K Liu, Y. Zhang, R. Yu, J.-X. Zhu, J.J. Lee, R.G. Moore, F.T. Schmitt, W. Li, S.C. Riggs, J.-H. Chu, B. Lv, J. Hu, M. Hashimoto, S.-K. Mo, Z. Hussain, Z.Q. Mao, C.W. Chu, I.R. Fisher, Q. Si, Z.-X. Shen and D.H. Lu, *Observation of temperature-induced crossover to an orbital-selective Mott phase in AxFe2-ySe2 (A=K, Rb) superconductors* (2015).

[82] X. Ding, Y. Pan, H. Yang and H.-H. Wen, *Strong and nonmonotonic temperature dependence of Hall coefficient in superconducting KxFe2-ySe2 single crystals* (2014).

[83] P. Gao, R. Yu, L. Sun, H. Wang, Z. Wang, Q. Wu, M. Fang, G. Chen, J. Guo, C. Zhang, D. Gu, H. Tian, J. Li, J. Liu, Y. Li, X. Li, Q. Si and Z. Zhao, *Role of the 245 phase in alkaline iron selenide superconductors revealed by high-pressure studies* (2014).

[84] Z. Wang, M. Schmidt, J. Fischer, V. Tsurkan, M. Greger, D. Vollhardt, A. Loidl and J. Deisenhofer, *Orbital-selective metal–insulator transition and gap formation above TC in superconducting Rb1-xFe2-ySe2* (2014).

[85] C. Zhang, W. Li and M. Xiao, *Mott behavior in KxFe2-ySe2 superconductors revealed by pump-probe spectroscopy* (2015).

[86] S. Lafuerza, H. Gretarsson, F. Hardy, T. Wolf, C. Meingast, G. Giovannetti, M. Capone, A. S. Sefat, Y.-J. Kim, P. Glatzel, and L. de' Medici, *Evidence of Mott physics in iron pnictides from x-ray spectroscopy* (2017).

[87] E. Bascones, B. Valenzuela and M. J. Calderón, *Magnetic interactions in iron superconductors: A review* (2016).

[88] L. Fanfarillo and E. Bascones, *Electronic correlations in Hund metals* (2015).

[89] V. Balédent, F. Rullier-Albenque, D. Colson, J.M. Ablett and J.-P. Rueff, *Electronic Properties of BaFe2As2 upon Doping and Pressure: The Prominent Role of the As p Orbitals* (2015).

[90] A. F. Kemper, T. A. Maier, S. Graser, H-P. Cheng, P. J. Hirschfeld and D. J. Scalapino, *Sensitivity of the superconducting state and magnetic susceptibility to key aspects of electronic structure in ferropnictides* (2010).

[91] M. D. Watson, P. Dudin, L. C. Rhodes, D. V. Evtushinsky, H. Iwasawa, S. Aswartham, S. Wurmehl, B. Büchner, M. Hoesch and T. K. Kim, *Probing the reconstructed Fermi surface of antiferromagnetic BaFe2As2 in one domain* (2019).

[92] X. F. Wang, T. Wu, G. Wu, H. Chen, Y. L. Xie, J. J. Ying, Y. J. Yan, R. H. Liu and X. H. Chen, *Anisotropy in the Electrical Resistivity and Susceptibility of Superconducting BaFe2As2 Single Crystals* (2009).

[93] N. Ni, A. Thaler, J. Q. Yan, A. Kracher, E. Colombier, S. L. Bud'ko, P. C. Canfield, and S. T. Hannahs, *Temperature versus doping phase diagrams for Ba(Fe$_{1-x}$TM$_x$)$_2$As$_2$ (TM=Ni,Cu,Cu/Co) single crystals* (2010).

[94] M. G. Kim, *Structural and magnetic properties of transition metal substituted BaFe2As2 compounds studied by x-ray and neutron scattering* (2012).

[95] X. Zhu, F. Han, G. Mu, J. Tang, J. Ju, K. Tanigaki and H.-H. Wen, *Superconductivity induced by doping Platinum in BaFe2As2* (2010).

[96] L. Li, H. Cao, M. A. McGuire, J. S. Kim, G. R. Stewart and Athena S. Sefat, *Role of magnetism in superconductivity of BaFe2As2: Study of 5d Au-doped crystals* (2015).

[97] G. S. Tucker, D. K. Pratt, M. G. Kim, S. Ran, A. Thaler, G. E. Granroth, K. Marty, W. Tian, J. L. Zarestky, M. D. Lumsden, S. L. Bud'ko, P. C. Canfield, A. Kreyssig, A. I. Goldman and R. J. McQueeney, *Competition between stripe and checkerboard magnetic instabilities in Mn-doped BaFe2As2* (2012).

[98] A. Thaler, H. Hodovanets, M. S. Torikachvili, S. Ran, A. Kracher, W. Straszheim, J. Q. Yan, E. Mun and P. C. Canfield, *Physical and magnetic properties of Ba(Fe1-xMnx)2As2 single crystals* (2011).

[99] K. Marty, A. D. Christianson, C. H. Wang, M. Matsuda, H. Cao, L. H. VanBebber, J. L. Zarestky, D. J. Singh, A. S. Sefat and M. D. Lumsden, *Competing magnetic ground states in nonsuperconducting Ba(Fe1-xCrx)2As2 as seen via neutron diffraction* (2011).

[100] X.-G. Li, J.-M. Sheng, C.-K. Tian, Y.-Y. Wang, T.-L. Xia, L. Wang, F. Ye, W. Tian, J.-C. Wang, J.-J. Liu, *Effects of vanadium doping on BaFe2As2* (2018).

[101] Y. Wang, J. E. Saal, S. L. Shang, X. D. Hui, L. Q. Chen and Z. K. Liu, *Effects of spin structures on Fermi surface topologies in BaFe$_2$As$_2$* (2011).

[102] J. Paglione and R. L. Greene, *High-temperature superconductivity in iron-based materials* (2010).

[103] T. M. Garitezi, C. Adriano, P. F. S. Rosa, E. M. Bittar, L. Bufaiçal, R. L. de Almeida, E. Granado, T. Grant, Z. Fisk, M. A. Avila, R. A. Ribeiro, P. L. Kuhns, A. P. Reyes, R. R. Urbano and P. G. Pagliuso, *Synthesis and Characterization of BaFe2As2 Single Crystals Grown by In-flux Technique* (2013).

[104] J. Halpern, *Atomic Orbitals* (2019).

[105] A. C. Moreira , C. R. Appoloni, *Mass attenuation coefficient of the Earth, Moon and Mars samples over 1keV-100GeV energy range* (2006).

[106] J. H. Hubbell and S. M. Seltzer, *X-Ray Mass Attenuation Coefficients* (2004).

[107] D. Pitzl, *Detectors for Particle Physics* (2011).

[108] A. L. Tenderholt, *Diagram showing which transitions contribute to X-ray absorption edges* (2015).

[109] R. Ortega, A. Carmona, I. Llorensc and P. L. Solaric, *X-ray absorption spectroscopy of biological samples. A tutorial* (2012).

[110] M. Blank, *Example XAS spectrum showing the three major data regions* (2010).

[111] D. Schulze, S. Anderson, S. Mattigod *et al.*, *Synchrotron x-ray sources and new opportunities in the soil and environmental sciences: Workshop report* (1990).

[112] G. S. Henderson, F. M. F. de Groot and B. J. A. Moulton, *X-ray Absorption Near-Edge Structure (XANES) Spectroscopy* (2014).

[113] A. Mesquita, A. Michalowicz and V.R. Mastelaro, *XANES measurements probing the local order and electronic structure of Pb1xBaxZr0.40Ti0.60O3 ferroelectric materials* (2015).

[114] J. Stöhr, *Magnetism: From Fundamentals to Nanoscale Dynamics*, 1st Ed., Springer Series in Solid-State Sciences (2006).

[115] K. Landskron, *Bonding in Coordination Compounds* (2011).

[116] F. de Groot, G. Vankó and P. Glatzel, *The 1s x-ray absorption pre-edge structures in transition metal oxides* (2009).

[117] R. Z. El-Kelma, L. Beldi, F. E. H. Hassan, G. Murtaza, R. Khenata, M. S. Abu-Jafar, S. B. Omran and B. Bouhafs, *Magnetic ordering and electronic structure of the ternary iron arsenide BaFe2As2* (2015).

[118] F. Peyrin, *Investigation of bone with synchrotron radiation imaging: From micro to nano* (2009).

[119] F. A. Lima, M. E. Saleta, R. J. S. Pagliuca, M. A. Eleotério, R. D. Reis, J. Fonseca Júnior, B. Meyer, E. M. Bittar, N. M. Souza-Neto and E. Granado, *XDS: a flexible beamline for X-ray diffraction and spectroscopy at the Brazilian synchrotron* (2016).

[120] A. L. Ankudinov, B. Ravel, J. J. Rehr, and S. D. Conradson, *Real-space multiple-scattering calculation and interpretation of x-ray-absorption near-edge structure* (1998).

[121] J. J. Kas, K. Jorissen and J. J. Rehr, *Real-Space Multiple-Scattering Theory of X-Ray Spectra* (2016).

[122] J. P. W. Bridgman, *The Physics of High Pressure* (1931).

[123] C. E. Weir, E. R. Lippincott, A. Van Valkenburg and E. N. Bunting, *Infrared Studies In the 1- to I5-Micron Region to 30,000 Atmospheres* (1959).

[124] N. Waeselmann, *Structural transformations in complex perovskite-type relaxor and relaxor-based ferroelectrics at high pressures and temperatures* (2012).

[125] J. Liu, *High pressure x-ray diffraction techniques with synchrotron radiation* (2016).

[126] N. Dubrovinskaia, L. Dubrovinsky, N. A. Solopova, A. Abakumov, S. Turner, M. Hanfland, E. Bykova, M. Bykov, C. Prescher, V. B. Prakapenka, S. Petitgirard, I. Chuvashova, B. Gasharova, Y.-L. Mathis, P. Ershov, I. Snigireva, A. Snigirev, *Terapascal static pressure generation with ultrahigh yield strength nanodiamond* (2016).

[127] A. S. Sefat, R. Jin, M. A. McGuire, B. C. Sales, D. J. Singh and D. Mandrus, *Superconductivity at 22 K in Co-Doped BaFe$_2$As$_2$ Crystals* (2008).

[128] J. S. Kim, S. Khim, H. J. Kim, M. J. Eom, J. M. Law, R. K. Kremer, J. H. Shim and Kee Hoon Kim, *Electron-hole asymmetry in Co- and Mn-doped SrFe$_2$As$_2$* (2010).

[129] Y. Singh, A. Ellern and D. C. Johnston, *Magnetic, transport, and thermal properties of single crystals of the layered arsenide BaMn$_2$As$_2$* (2009).

[130] Y. Singh, M. A. Green, Q. Huang, A. Kreyssig, R. J. McQueeney, D. C. Johnston and A. I. Goldman, *Magnetic order in BaMn$_2$As$_2$ from neutron diffraction measurements* (2009).

[131] A. S. Sefat, D. J. Singh, R. Jin, M. A. McGuire, B. C. Sales and D. Mandrus, *Renormalized behavior and proximity of BaCo$_2$As$_2$ to a magnetic quantum critical point* (2009).

[132] V. K. Anand, D. G. Quirinale, Y. Lee, B. N. Harmon, Y. Furukawa, V. V. Ogloblichev, A. Huq, D. L. Abernathy, P. W. Stephens, R. J. McQueeney, A. Kreyssig, A. I. Goldman, and D. C. Johnston, *Crystallography and physical properties of BaCo$_2$As$_2$,Ba$_0$.94K$_0$.06Co$_2$As$_2$, and Ba$_0$.78K$_0$.22Co$_2$As$_2$* (2014).

[133] J. Pelliciari, K. Ishii, L. Xing, X. Wang, C. Jin and T. Schmitt, *Fluctuating magnetism of Co- and Cu-doped NaFeAs* (2021).

[134] J. Cheng, P. Dong, W. Xu, S. Liu, W. Chu, X. Chen and Z. Wu, *Charge redistribution and a shortening of the Fe-As bond at the quantum critical point of SmO$_{1-x}$F$_x$FeAs* (2015).

[135] W. Chu, J. Cheng, S. Chu, T. Hu, A. Marcelli, X. Chen and Z. Wu, *Iron Isotope Effect and Local Lattice Dynamics in the (Ba, K)Fe$_2$As$_2$ Superconductor Studied by Temperature-Dependent EXAFS* (2013).

[136] W. Xu, A. Marcelli, B. Joseph, A. Iadecola, W. S. Chu, D. Di Gioacchino, A. Bianconi, Z. Y. Wu and N. L. Saini, *Local structural disorder in REFeAsO oxypnictides by RE L$_3$ edge XANES* (2010).

[137] B. Joseph, A. Ricci, N. Poccia, V. G. Ivanov, A. A. Ivanov, A. P. Menushenkov, N. L. Saini and A. Bianconi, *Temperature-Dependent As K-Edge EXAFS Studies of LaFe$_{1-x}$Co$_x$AsO (x = 0.0 and 0.11) Single Crystals* (2016).

[138] M. Y. Hacisalihoglu, E. Paris, B. Joseph, L. Simonelli, T. J. Sato, T. Mizokawah and N. L. Saini, *A study of temperature dependent local atomic displacements in a Ba(Fe$_{1-x}$Co$_x$)$_2$As$_2$ superconductor* (2016).

[139] C. L. Chen, S. M. Rao, C. L. Dong, J. L. Chen, T. W. Huang, B. H. Mok, M. C. Ling, W. C. Wang, C. L. Chang and T. S. Chan, *X-ray absorption spectroscopy investigation of the electronic structure of superconducting FeSe$_x$ single crystals* (2011).

[140] C. L. Chen, C. L. Dong, J. L. Chen, J.-H. Guo, W. L. Yang, C. C. Hsu, K. W. Yeh, T. W. Huang, B. H. Mok, T. S. Chan, J. F. Lee, C. L. Chang, S. M. Raoa and M. K. Wu, *X-Ray spectra and electronic correlations of FeSe$_{1-x}$Te$_x$* (2011).

[141] B. C. Chang, Y. B. You, T. J. Shiu, M. F. Tai, H. C. Ku, Y. Y. Hsu, L. Y. Jang, J. F. Lee, Z. Wei, K. Q. Ruan, and X. G. Li, *Angular dependence of x-ray absorption spectrum for field-aligned iron-based superconductors* (2009).

[142] B. Joseph, A. Iadecola, L. Simonelli, Y. Mizuguchi, Y. Takano, T. Mizokawa and N. L. Saini, *A study of the electronic structure of FeSe$_{1-x}$Te$_x$ chalcogenides by Fe and Se K-edge x-ray absorption near edge structure measurements* (2010).

[143] S. I. Zabinsky, J. J. Rehr, A. Ankudinov, R. C. Albers, and M. J. Eller, *Multiple-scattering calculations of x-ray-absorption spectra* (1995).

[144] J. J. Rehr and R. C. Albers, *Theoretical approaches to x-ray absorption fine structure* (2000).

[145] F. Neese, *The ORCA program system* (2000).

[146] F. Neese, *Software update: the ORCA program system, version 4.0* (2017).

[147] F. A. Garcia, O. Ivashko, D. E. McNally, L. Das, M. M. Piva, C. Adriano, P. G. Pagliuso, J. Chang, T. Schmitt and C. Monney, *Anisotropic magnetic excitations and incipient Néel order in Ba(Fe$_{1-x}$Mn$_x$)$_2$As$_2$* (2019).

[148] P. F. S. Rosa, C. Adriano, T. M. Garitezi, M. M. Piva, K. Mydeen, T. Grant, Z. Fisk, M. Nicklas, R. R. Urbano, R. M. Fernandes and P. G. Pagliuso, *Possible unconventional superconductivity in substituted BaFe$_2$As$_2$ revealed by magnetic pair-breaking studies* (2014).

[149] L. Hedin and B. I. Lundqvist, *Explicit local exchange-correlation potentials* (1971).

[150] S. K. Singh, J. Eng, M. Atanasov and F. Neese, *Covalency and chemical bonding in transition metal complexes: An ab initio based ligand field perspective* (2017).

[151] P. Norman and A. Dreuw, *Simulating X-ray Spectroscopies and Calculating Core-Excited States of Molecules* (2018).

[152] H. Suzuki, T. Yoshida, S. Ideta, G. Shibata, K. Ishigami, T. Kadono, A. Fujimori, M. Hashimoto, D. H. Lu, Z.-X. Shen, K. Ono, E. Sakai, H. Kumigashira, M. Matsuo, and T. Sasagawa, *Absence of superconductivity in the hole-doped Fe pnictide Ba(Fe$_{1-x}$Mn$_x$)$_2$As$_2$: Photoemission and x-ray absorption spectroscopy studies* (2013).

[153] Y. Texier, Y. Laplace, P. Mendels, J. T. Park, G. Friemel, D. L. Sun, D. S. Inosov, C. T. Lin and J. Bobroff, *Mn local moments prevent superconductivity in iron pnictides Ba(Fe$_{1-x}$Mn$_x$)$_2$As$_2$* (2012).

[154] T. Kobayashi, M. Nakajima, S. Miyasaka, and S. Tajima, *Carrier localization due to local magnetic order induced by magnetic impurities in Ba(Fe$_{1-x}$TM$_x$)$_2$As$_2$ (TM = Mn and Cr) as seen via optical spectra* (2016).

[155] M. Merz, P. Schweiss, P. Nagel, M.-J. Huang, R. Eder, T. Wolf, H. von Löhneysen, S. Schuppler, *Of Substitution and Doping: Spatial and Electronic Structure in Fe Pnictides* (2016).

[156] M. Nakajima, M. Nagafuchi, and S. Tajima, *Comprehensive study of out-of-plane transport properties in BaFe$_2$As$_2$: Three-dimensional electronic state and effect of chemical substitution* (2018).

[157] M. A. Tanatar, N. Ni, A. Thaler, S. L. Bud'ko, P. C. Canfield, and R. Prozorov, *Systematics of the temperature-dependent interplane resistivity in Ba(Fe$_{1-x}$M$_x$)$_2$As$_2$ (M=Co, Rh, Ni, and Pd)* (2011).

[158] S. Thirupathaiah, S. de Jong, R. Ovsyannikov, H. A. Dürr, A. Varykhalov, R. Follath, Y. Huang, R. Huisman, M. S. Golden, Yu-Zhong Zhang, H. O. Jeschke, R. Valentí, A. Erb, A. Gloskovskii, and J. Fink, *Orbital character variation of the Fermi surface and doping dependent changes of the dimensionality in BaFe$_{2-x}$Co$_x$As$_2$ from angle-resolved photoemission spectroscopy* (2010).

[159] J. Pelliciari, K. Ishii, Y. Huang, M. Dantz, X. Lu, P. O.-Velasco, V. N. Strocov, S. Kasahara, L. Xing, X. Wang, C. Jin, Y. Matsuda, T. Shibauchi, T. Das and T. Schmitt, *Reciprocity between local moments and collective magnetic excitations in the phase diagram of BaFe2(As$_{1-x}$P$_x$)$_2$* (2019).

[160] K. Haule and G. Kotliar, *Coherence–incoherence crossover in the normal state of iron oxypnictides and importance of Hund's rule coupling* (2009).

[161] S. Alvarez and J. Cirera, *How High the Spin? Allowed and Forbidden Spin States in Transition-Metal Chemistry* (2006).

[162] R. K. Hocking and E. I. Solomon, *Ligand Field and Molecular Orbital Theories of Transition Metal X-ray Absorption Edge Transitions* (2011).

[163] A.-R. Allouche, *Gabedit—A graphical user interface for computational chemistry softwares* (2010).

[164] T. Lu and F. Chen, *Multiwfn: A multifunctional wavefunction analyzer* (2011).